Original Article

Corresponding author:
Martin B Klausen; Email: klausen@sun.ac.za

![CAMBRIDGE UNIVERSITY PRESS]

Diversification inside a lamprophyric dyke and cone sheet complex converging onto a hidden carbonatite centre (Frederikshåbs Isblink, SW Greenland)

Martin Bromann Klausen[1,2] 🄳 and Madelaine R Frazenburg[3]

[1]Department of Earth Sciences, Stellenbosch University, Matieland, Stellenbosch, South Africa; [2]Geological Survey of Denmark & Greenland, Copenhagen, Denmark and [3]Central Analytical Facility, Stellenbosch University, Matieland, Stellenbosch, South Africa

Abstract

Both radiating dykes and proximal cone sheets converge onto a positive aeromagnetic anomaly of an inferred carbonatitic centre, hidden beneath a retreating edge of the Frederikshåbs Isblink glacier. This convergence, together with sub-parallel incompatible element patterns by all intrusions, suggests a cogenetic relationship that warrants investigation into potential diversification processes. More primitive high- and low-Mg damtjernites, which for three dykes conform to more porphyritic dyke cores and aphyric margins, respectively, can be explained by high-Mg trends being controlled by the fractionation/accumulation of mainly augite and olivine (or other mafic phases), while discordant low-Mg trends require additional decoupled magnetite fractionation. It is proposed that each dyke intrusion tapped the differentiated top of a central magma chamber, occasionally followed by an unconsolidated mafic cumulate mush, excluding denser magnetites, with *in situ* flow segregation playing a subordinate additional role. Beyond the most differentiated damtjernite, more evolved phonolitic nephelinites to carbonaceous alnöites split into bulk rock geochemical T-trends that can only relate to late-stage segregations into magmas with varying proportions of interstitial igneous (not secondary) analcime and carbonate – collectively increasing in volume with differentiation. While the analcime component also appears to segregate more readily into veins and ocelli than carbonatite, it is speculated if such low viscosity, density and liquidus rest melts, inside igneous centres, more efficiently aggregated into voluminous, buoyant analcime caps above slightly denser carbonatites. Similar converging plumbing systems and diversification processes are proposed for other complexes, where kimberlitic parents were simply extracted from deeper mantle sources.

1. Introduction

Hypabyssal lamprophyre intrusions and associated carbonatites are found in a variety of different tectonic settings (e.g., Woolley & Kjarsgaard, 2008) and are renowned for their debated origins and complicated nomenclature, where Rock (1987, 1991) initially introduced the term 'lamprophyre clan' to encompass lamproites and kimberlites. The scientific community has since, however, settled on treating the petrogenesis of these rock types independently (e.g., Mitchell, 1994; Woolley *et al.* 1996; Le Maitre, 2002; Tappe *et al.* 2005, 2021). Calc-alkaline lamprophyres, including appinites (Murphy, 2013) and more leucite-bearing varieties, are more common within supra-subduction zones, orogenic and especially post-orogenic settings, shared by lamproites. More sodic alkali and ultramafic lamprophyres are on the other hand intraplate to rift-related and more relevant to this paper. Among these, alkali lamprophyres may be regarded as hydrous basanites, whereas ultramafic lamprophyres typically have less silica ($SiO_2 < 35$ wt%) and are most intimately associated with kimberlites.

Alkali and ultramafic lamprophyres are, together with kimberlites, in many ways scientifically intriguing. Foremost, by offering important insight into exotic and deep mantle petrogenesis (e.g., Brey *et al.* 2008; Giuliani *et al.* 2020), where there is a growing consensus that such magmas are derived from deep, sub-continental and metasomatized (including carbonated) lithospheric mantle sources (Tappe *et al.* 2011, 2017a), but also include primary asthenospheric magmas that interact with the lithosphere, *en route* towards the Earth's surface (e.g., Stamm & Schmidt, 2017; Pearson *et al.* 2019). When it comes to associated carbonatites (Kamenetsky *et al.* 2021; Yaxley *et al.* 2022), a plethora of processes have been offered to explain their formation, including (1) liquid–liquid immiscibility (e.g., Hamilton *et al.* 1979; Foley, 1984; Bell, 1989 and chapters therein; Brooker, 1998; Bell *et al.* 1999; Brooker & Kjarsgaard, 2011), (2) a more direct derivation from carbonated mantle sources (e.g., Harmer & Gittins, 1998; Mitchell, 2005), and (3) fractional crystallization of associated lamprophyres or kimberlites (e.g.,

Tappe et al. 2017a; Weidendorfer et al. 2017). A further linking of petrogenetically related units within individual complexes through magma differentiation has in contrast received less attention (exceptions being Ivanikov et al. 1998; Nosova et al. 2021a), despite remarkably low-melt viscosities of such volatile-rich and low-silica magmas speeding up fractionation processes.

This paper delves deeper into the field relationships, petrography and both mineral and bulk rock geochemistry of lamprophyric to more evolved radiating dykes and cone sheets, which all appear to have been injected from a common igneous centre that coincides with a distinct positive aeromagnetic anomaly, resembling other carbonatitic centres across southern West Greenland. Since a cogenetic relationship between all units is further supported by shared interstitial mineralogy and similar incompatible element signatures, we link these through a sequence of diversification processes from a common parent, seemingly leading to the segregation of immiscible analcimic and carbonatitic rest melts.

2. Geological setting

The studied ~150 Ma cluster of lamprophyric to even more evolved dykes and sheets at Frederikshåbs Isblink (FHI), including a 152.1 ± 1.6 Ma U-Pb perovskite age in Larsen et al. (2009), form part of a Neoproterozoic to Mesozoic Province of otherwise mostly calcite kimberlites, ultramafic lamprophyres and associated carbonatites that scatter as dispersed clusters across much of the eastern Canadian Shield (e.g., Heaman & Kjarsgaard, 2000; Tappe et al. 2017a,b), including southern West Greenland.

2.a. A Mesozoic Labrador Sea sub-province

Modified from Steenfelt et al. (2006), Fig. 1(a) shows that a greater abundance of lamprophyre/kimberlite intrusions (orange dots) and associated carbonatite centres (yellow pentagons) outcrop across southern West Greenland, compared to along its conjugate Labrador margin (Sinclair et al. 2002; Wilton et al. 2002; Tappe et al. 2006), even if the latter includes the Aillik Bay complex, as the type locality for aillikites. This bias may relate to Greenland being underlain by a thicker and more fertile/carbonated Archaean core, whereas Labrador is truncated by a Paleoproterozoic Core Zone and incorporates a greater abundance of Mesoproterozoic batholiths. The bias could also relate to asymmetric Jurassic-Cretaceous rifting (Tappe et al. 2006), eventually leading to a Paleogene opening of the Labrador Sea, along which progressively more feldspar-bearing, alkali to eventually even tholeiitic magmas were emplaced (Tappe et al. 2007; Larsen et al. 2009).

Focusing on the Mesozoic, much research addresses petrogenetic aspects (e.g., Tappe et al., 2011, 2017a) – tentatively attributed to a subducted Pacific plate (Kjarsgaard et al. 2017; Tappe et al. 2013), regional rifting (Tappe et al. 2014, 2017b) and a Great Meteor hot spot track (Heaman & Kjarsgaard, 2000) – as well as its entrained diamonds (e.g., Kjarsgaard, 2007). It is debatable, however, whether a mantle plume head of a maximum ~1000 km radius (White & McKenzie, 1995) triggered the Mesozoic Labrador Sea lamprophyre–kimberlite–carbonatite sub-province, because (1) an extrapolation of Lawver and Müller's (1994) proto-Icelandic hot spot track at ~150 Ma roughly positions that plume centre north of Greenland, requiring ~1700 km of lateral mantle plume flow to the nearest Mesozoic Tupertalik complex (Fig. 1), and (2) a ~150 Ma Great Meteor plume centre near a more kimberlite-dominated Kirkland Lake – Timiskaming area (Heaman &

Kjarsgaard, 2000) would have been located at an even greater radial distance of ~1800 km from the west coast of Greenland. Since edge-driven convection, proposed for younger kimberlites along the western edge of the Canadian Shield (Kjarsgaard et al. 2017), unlikely played a role this far east of a subducting Farallon plate, it remains to be shown if lithospheric rifting was sufficient – on its own – to induce Mesozoic lamprophyre–kimberlite magmatism across the Labrador Sea sub-province.

2.b. Dyke and sheet clusters around common magmatic centres

Previous mapping of the Labrador Sea sub-province has identified clusters of calcite kimberlites and lamprophyres that occasionally surround coeval carbonatites (e.g., Steenfelt et al. 2006). Apart from radiating dykes converging onto some offshore Aillik Bay centre (cf., Fig. 2 in Tappe et al. 2006), however, other complexes have not been related to any plumbing system, let alone to associated carbonatites, where FHI's radiating dyke swarm and centrally inclined cone sheets towards an inferred carbonatite in Fig. 1(a) are all contributions from this study, as presented in more detail in Fig. 2(e). That geological map further includes an aeromagnetic map, superimposed onto the FHI glacier and colour-coded according to the legend's total magnetic intensity (TMI) scale, that exhibits a distinct positive anomaly (up to ~400 nT) at the southern edge of the glacier, towards which all studied dykes (in red) and inclined sheets (in green) converge.

Such conspicuous convergence – as traced from 100:000 scale geological maps (Fig. 2e) and mapped within study areas S, C & N in 2010 (Fig. 2e-g) – conforms to how Chadwick & Dieterich (1991) model a similar combined radiating dyke and circumferential cone sheet swarm on a Galapagos Island. In their model, a mushroom-shaped central magma source (Fig. 2h) generates a combined local stress field, in which an over-pressurized cylindrical stem triggers the injection of radiating dykes, while concentric and centrally inclined sheets are injected from its oblate crown. It remains to be seen if FHI's radiating dykes are limited to the northern side of its proposed centre or other associated dykes can also be mapped and sampled to the south of that centre. For the latter, the nearest Paamiut dykes are deemed too distally located (Fig. 1a), too ultramafic (cf., later Fig. 8a) and too old (~166 Ma) to have been injected from the same FHI centre.

Purely based on similarities with the aeromagnetic anomalies at four known carbonatite complexes along the southern west coast of Greenland (Fig. 1), shown at similar scales in Fig. 2(a-d) for comparisons, it is tempting to propose that the FHI anomaly/centre is likewise carbonatitic, at least as a working hypothesis for this paper. Even if the FHI anomaly does not exhibit any anomalously low nT-rim – like the one around the Neoproterozoic Sarfartoq carbonatite (Fig. 3a), likely reflecting how its demagnetized fenitized host rocks contrast its magnetite-rich carbonatite centre – the other verified carbonatite examples argue that such low-magnetic rims are not prerequisite. Thus, even if unavailable gravimetric or radiometric data would strengthen interpretations (Thomas et al. 2016), available evidence allows the FHI anomaly to be a carbonatite centre that – due to its combined glacial cover and proximity to the sea – may have been missed by both geological and stream sediment mappers (cf., Steenfelt et al. 2009, for the latter).

If the FHI anomaly turns out to be a carbonatitic centre, this would follow upon another recent discovery of an almost coeval and neighbouring Tikiusaaq carbonatite (Steenfelt et al. 2006; Fig. 2c). As illustrated in Fig. 1(a), it would also result in a conspicuous regular
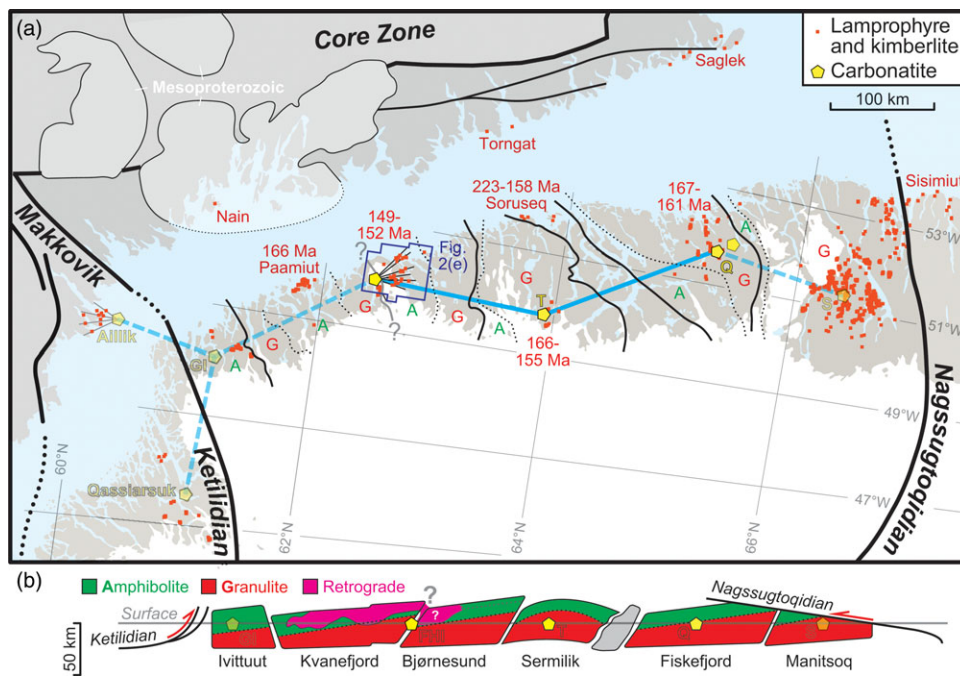
Figure 1. (Colour online) (a) Mesozoic reconstruction, showing lamprophyre, kimberlite (both as orange dots) and carbonatite (yellow pentagon) locations across an Archaean North Atlantic Craton of southern W Greenland and E Labrador (modified from Steenfelt *et al*. 2006), where Neoproterozoic carbonatite centres are subdued. Ages are from Larsen *et al*. (2009). As argued in the paper, lamprophyre dykes converge onto an inferred FHI carbonatite centre, like Aillik dykes (Tappe *et al*. 2006). Craton is bound to the north and south by Paleoproterozoic orogens in paler shades of grey and Mesoproterozoic units to the east in even paler shades. Paleotectonic domains and Archaean terranes separated by solid black lines, whereas dotted lines separate systematic southern amphibolite to northern granulite facies shifts across Archaean terrane blocks, as defined by Windley & Garde (2009). (b) Their crustal cross section, onto which are added Ketilidian and Nagssugtoquidian thrusts from Garde *et al*. (2002) and van Gool *et al*. (2002), respectively. GI = Grønnedal-Ika, FHI = Frederiks Håb Isblink, T = Tikiusaaq, Q = Qaqarsuuk, S = Sarfartoq.
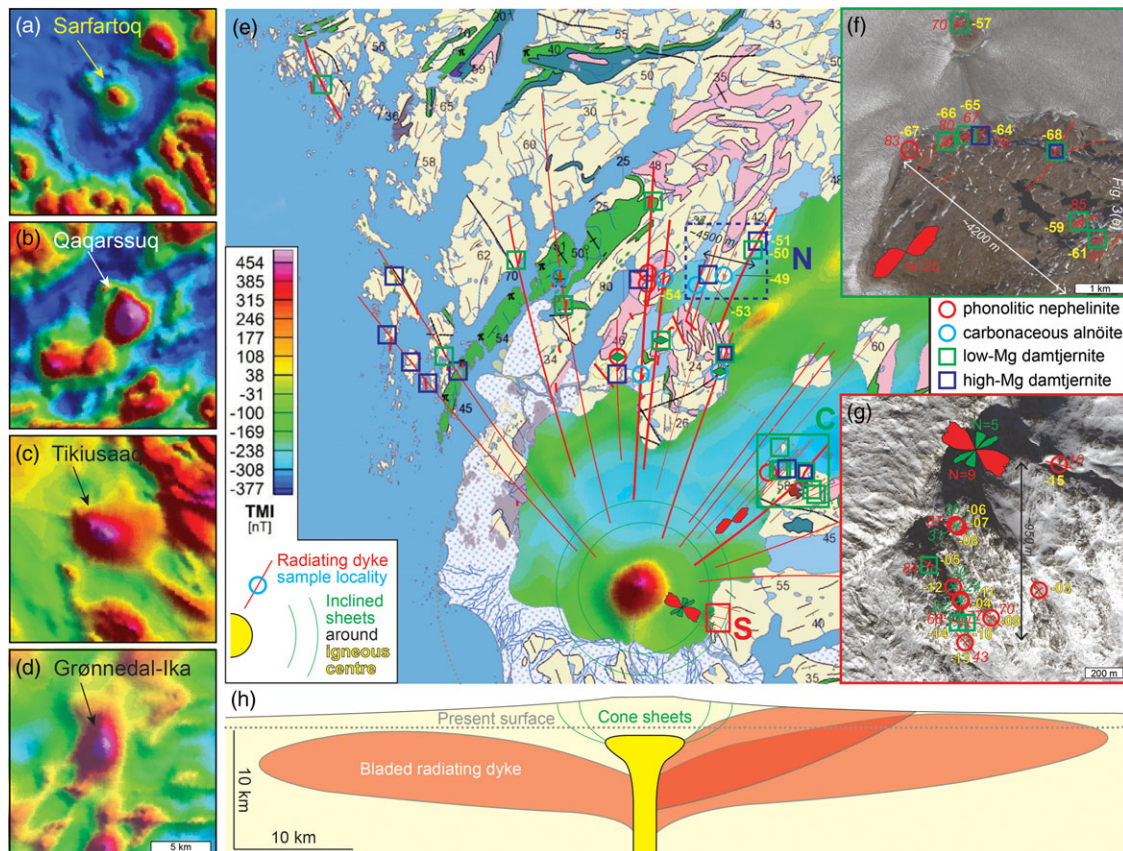

Figure 2. (Colour online) Field relationships. (a-d) AEROMAG TMI (1996) extracts (copied from Naalakkersuisut's 'Greenland Portal') of four known carbonatite centres along the southern west coast of Greenland, compared to (e) glaciated areas inside 1:100 000 geological map of outcropping area (Kokfelt *et al*., 2019). Twenty-two published and 25 new dyke, sheet and sill sampling localities are shown, using colours and symbols as in Fig. 8. Moving average rose diagrams for dyke (red) strike measurements from the central (C) and southern (S) study area, converge – together with inclined sheet (green) dip directions – onto a positive aeromagnetic anomaly (up to 400 nT). (f-g) Google Earth images of study areas C and S, onto which this paper's sampled dykes and inclined sheets are located and where each sample number terminates a 5197-prefix. (h) Conceptional cross section through how a mushroom-shaped igneous centre (yellow) gives rise to a local stress field that allows the injection of both bladed radiating dykes from its cylindrical stem, as well as inclined cone sheets from the crown of a more oblate head.

Figure 3. (Colour online) Field photos: (a) a westerly view across study area S, intruded by both radiating dykes and shallow W-dipping sheets, both of which converge onto an aeromagnetic anomaly that is located at the edge of the FHI glacier, ~6.5 km behind this outcrop. Each sample number terminates a 5197-prefix. (b) Weakly biotite-phyric 519705 LMD-dyke. (c) Inclined 519704 PN-sheet. (d) A 2.4 m-thick damtjernite dyke, located ~28 km from the aeromagnetic anomaly in Fig. 2(e), from which a more aphyric LMD margin (519750) and more porphyritic HMD core (519751) was sampled. (e) A 0.2 m-thick and 64° SW-dipping dyke from the central area (not sampled), with numerous margin-parallel ocelli strands that plunge down-dip.

zig-zag 'chain' of carbonatitic centres across the Labrador Sea sub-province, with Mesozoic centres – emplaced during Pangea break-up – located 170–176 km apart across the core of the North Atlantic Craton, while more peripheral Neoproterozoic centres – emplaced during the assembly of Pangea – occur slightly closer (130–137 km) to each other and even inside Paleoproterozoic orogens that verge onto the craton from north and south.

Another note may be made on how all known carbonatite centres across the North Atlantic Craton, with their surrounding clusters of lamprophyres and kimberlites, appear restricted to the cores of lower-order Archaean craton blocks, as defined by Windley & Garde (2009), rather than along their boundaries (cf., Fig. 1a-b). While this could be used as an argument against the presence of a carbonatitic FHI centre, its existence could equally well question the boundary between a more northerly located Bjørnesund and southerly located Kvanefjord block, hidden by the particularly large FHI glacier. If so, Bjørnesund's southern amphibolite grade zone, which Windley & Garde (2009) use as an argument for a domino-block-like craton block boundary below the FHI glacier, may represent a northward extension of their retrogressed nappe covering parts of the Kvanefjord block (magenta unit in Fig. 1b).

3. Petrography

Around the aeromagnetic anomaly at FHI (Figs. 2e & 3a), most radiating dykes (Fig. 3b) and centrally inclined sheets (Fig. 3c) have a relatively low abundance of phenocrysts, yet often rounded whitish ocelli that were erroneously interpreted in the field as amygdales and thereby avoided during sampling. Two significantly thicker dykes, however, were found to have distinctly more porphyritic cores (Fig. 3d). As illustrated by, for example, DW Hawkins, unpub. MSc thesis, St John's Memorial Univ. Newfoundland, 1976, such strong compositional zoning is characteristic for many lamprophyric dykes and may reflect either flow segregation – further facilitated by a low viscosity of such silica-poor and volatile-rich magmas – and/or multiple pulses of variably aphyric to porphyritic magmas. In Fig. 3(d), one could also argue for a later injection of a moderately porphyritic zone into this dyke's aphyric margin. The presence of exclusively mafic (including hydrous) minerals and ocelli is another lamprophyre characteristic (e.g., Carstens, 1961; Ferguson & Currie, 1971; DW Hawkins, unpub. MSc thesis, St John's Memorial Univ. Newfoundland, 1976; Cooper, 1979; Foley, 1984; Mitchell, 1994; Fareeduddin et al. 2001; Nosova et al. 2021a,b), consistent with magmas having been volatile-rich. One inclined dyke in study area C

(Fig. 3e) was even observed to have an unusually large abundance of pipe ocelli (observed elsewhere by Dawson & Hawthorne, 1973; Tappe *et al.* 2014; Abersteiner *et al.* 2019) that plunge down dip and parallel to a likely upward flow direction. Unfortunately, no sample was collected from this dyke, because ocelli – as mentioned – were believed to be amygdales.

3.a. Petrographic classifications

During previous studies of the FHI complex, Hansen (1980) mainly distinguished between nephelinites and carbonate-bearing melilitites, where nephelinites were further sub-divided into being olivine-bearing and progressively more evolved than that. She also identified melilitites, where the central portion of one composite melilitite dyke (sample 118101) is even carbonatitic. In a systematic review of intrusions across southern West Greenland (Fig. 1a), Larsen *et al.* (2009) adopted a more petrographic classification scheme by Le Maitre (2002), relabelling Hansen's (1980) kaersutite-, Ti-rich augite-, olivine- and biotite-phyric nephelinites as monchiquites and her melilitites as alnöites. The latter is in accordance with Tappe *et al.* (2005), who argue for an addition of three ultramafic lamprophyre types into Le Maitre's (2002) classification scheme, namely (1) melilite-bearing alnöites, (2) less magnesian and more nepheline and/or alkali feldspar-bearing damtjernites and (3) more magnesian, carbonate-rich and garnet-bearing aillikites.

Since it will be shown that two dykes with porphyritic cores and almost aphyric margins neither contain melilite, leucite or garnet, but rather interstitial sodic foids, we reclassify the monchiquites by Larsen *et al.* (2009) as damtjernites, following Tappe *et al.* (2006) and Pandey *et al.* (2018). A further distinction between typically more porphyritic olivine damtjernites and often almost aphyric damtjernites will be supported by bulk rock geochemistry (Section 4.1) and here forthwith referred to as either high- or low-Mg damtjernites (abbreviated as HMD and LMD, respectively). It will also be shown how more evolved monchiquites by Larsen *et al.* (2009) host too much foids to classify as lamprophyres and thereby conform better to Hansen's nephelinites and may even be regarded as phonolitic (i.e., here forthwith referred to as phonolitic nephelinites (PN), or simply nephelinites for short). Finally, for the lack of a better name, we adopt alnöite from Larsen *et al.* (2009), even if these rocks may contain insufficient melilite and where we wish to stress their more carbonaceous nature (i.e., here forthwith referred to as carbonaceous alnöites (CA), or simply alnöites for short).

In the following sub-sections, microscope petrography and scanning electron microscope (SEM) mineral chemistry (Supplement A) focus on one sample from each of the four main rock types (HMD, LMD, alnöite and nephelinite). Due to space restrictions, an additional sample of each rock type is presented as Supplementary Material B, together with autolithic nodules (Fig. B4) from within a proximal LMD dyke (519714) in study area S (Figs. 2g & 3a). Thus, representing damtjernites, a better exposed and 2.4 m-thick distal dyke from study area N (Fig. 3d) was sampled from both its almost aphyric LMD margin (519750A) and more porphyritic and olivine-bearing HMD core (519750B), with another even more porphyritic core sample (519751) collected a farther 156 m NNW and along that same dyke (Fig. 2e). Representing a more evolved alnöite–nephelinite suite, identified geochemically in Section 4, this main paper includes the most carbonaceous, or least silicic, of two aphyric and radiating alnöite dykes (510754) from study area N (Fig. 2e), as well as a radiating

Table 1. Phenocryst assemblages within damtjernites

Sample (5197-)	-68M	-68C	-50A	-50B	-51
Rock type	LMD	HMD	LMD	HMD	HMD
% of thin section	2.9	47.3	1.4	26.7	42.0
Olivine	1.8	27.2		5.7	6.4
Augite	76.3	72.2	62.3	54.5	53.3
Magnetite	21.8	0.6	34.7	8.8	7.7
Kaersutite				2.6	11.2
Biotite			2.9	27.5	21.5
Nepheline				0.9	

All proportions are out of 100%, excluding matrix and ocelli.

nephelinite dyke (519715), from inside the most proximal study area S (Fig. 2g).

3.b. Damtjernites

In Fig. B1, a pair of thin section slides of the porphyritic HMD core and almost aphyric LMD margin of the thickest dyke in this study (519768C & -M, respectively) quantify how locally touching euhedral olivine and a greater abundance of faintly beige coloured augite phenocrysts, together with rarer magnetite micro-phenocrysts, abound inside this dyke's HMD core (-68C in Table 1). These phenocrysts define a panidiomorphic texture, indicative of a cumulative origin. Even if shared assemblages in both margin and core samples are consistent with flow segregation, the marginal sample's 2.9% of (micro)phenocrysts record a greater proportion of magnetite and less olivine, compared to the more porphyritic dyke core, yet almost equal augite proportions (cf., −68M and −68C in Table 1). Phenocrysts exhibit little internal zonation, except for thin, darker and more titaniferous augite rims, where centrally positioned SEM spot analyses (Supplement A) were made on individual phenocrysts within the dyke's porphyritic HMD core. These results (Fig. B9) show that 20 olivine and 26 augite phenocrysts inside this dyke core (519768C) are the most magnesian among all analyses in this study (Fo_{88-80} and Di_{90-71}, respectively), which together with 20 more magnesian and aluminous magnetites are consistent with this dyke being more primitive than another damtjernite dyke with a porphyritic core (519750-1 in Fig. 3d), described next.

The three thin section scans in Fig. 4(a-c), together with additional traced copies in Fig. B2(a-c), quantify both phenocryst abundances and grain sizes (cf., Fig. B2d-f for the latter). These results (Table 1) show that this dyke's pair of porphyritic HMD core samples (collected 156 m apart along the same dyke) host roughly similar phenocryst assemblages, especially, after combining slightly paler brown kaersutites with darker brown and often more euhedral biotite phenocrysts. As supported by SEM spot analyses from the most porphyritic core sample 519751 (cf, small, colour-coded circles in Fig. 4c), with largest and freshest phenocrysts, this dyke core not only includes anhydrous olivines, augites and magnetites, like in the previous more primitive dyke, but also hydrous kaersutites and biotites, consistent with a more evolved composition. This is substantiated by less magnesian olivines (18 analyses of Fo_{84-78}) and augites (43 analyses of Di_{84-71}), while 11 kaersutite and 22 biotite spot analyses have Mg numbers ranging between 72-66 and 54-52, respectively (Fig. B9). In addition to magnetites also being less magnesian and aluminous
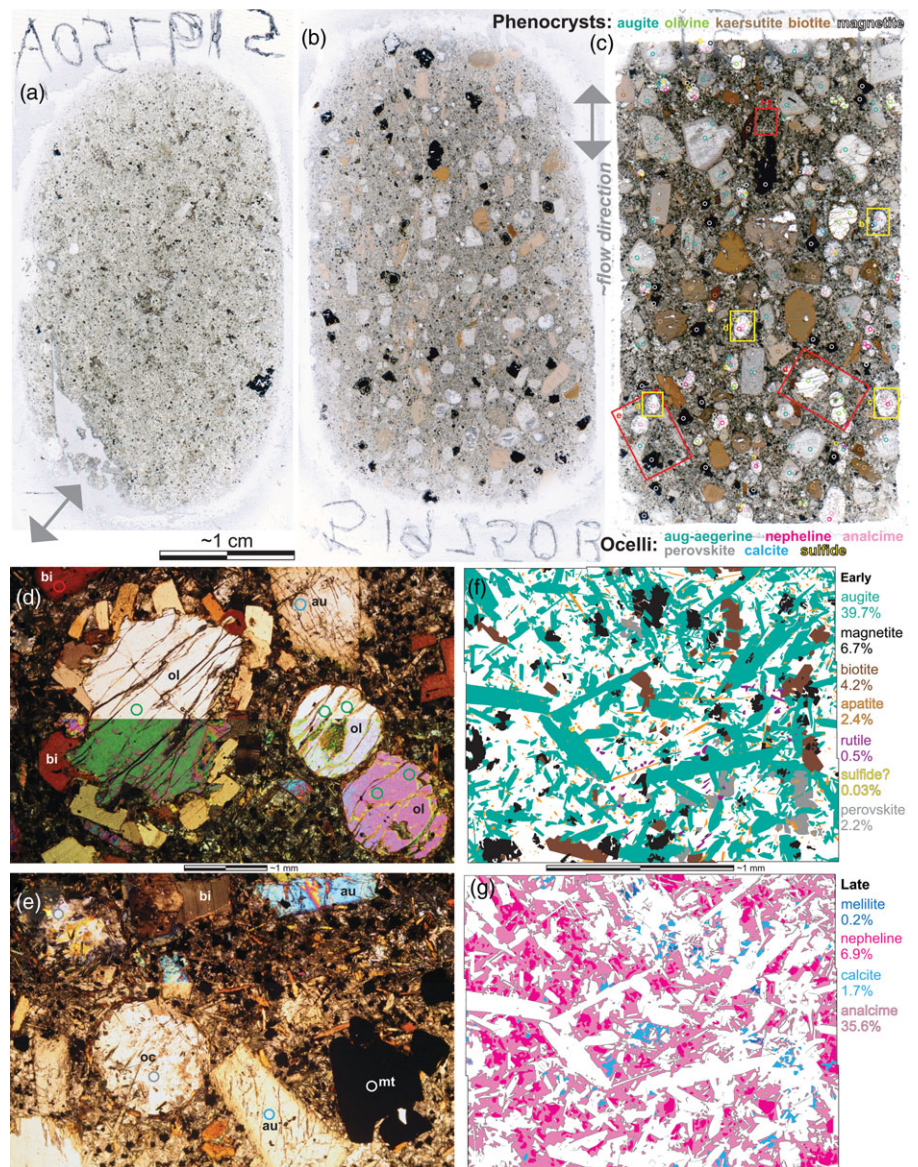
Figure 4. (Colour online) Damtjernite petrography. (a-c) Three thin section scans, where 519750A & -B (a & b, respectively) were collected next to each other and 519751 (c) was collected 156 m NNW along the same dyke. Colour-coded circles in (c) locate SEM spot analyses (Fig. B9). Red and yellow frames in (c) locate microphotos (d-e), matrix phase maps (f-g) and ocelli in Fig. 5(a-d). (d) Partly resorbed olivine (ol) phenocrysts, where one has a 'corona' of epitaxially overgrown euhedral biotites (bi). (e) Other phenocrysts, including augite (au) and magnetite (mt), together with circular and internally heterogeneous ocelli (oc). (f-g) 3.1 mm²-large matrix phase maps (cf., Fig. B3) for (f) more euhedral matrix crystals, forming a framework inside which (g) interstitial phases crystallized. Colour-coded text acts as a legend, quantifying modal proportions.

than in sample 519768C, sample 519751 – by chance – also hosts a single and anomalously large ilmenite, likely as a xenocryst.

Even if phenocrysts are not conducive towards interpretations of crystallization sequences, the presence of only anhydrous olivines, augites and magnetites in the more primitive HMD sample 519768C argues for these being the earliest crystallizing phases. The addition of both kaersutite and biotite phenocrysts in the more evolved HMD samples 519750-1 indicates that early crystallizing anhydrous phases were followed by more hydrous phases, reflecting a P_{H2O} increase during early differentiation. In addition, conspicuously rounded olivine (and to a lesser extent also kaersutite) phenocrysts are resorbed (e.g., lower right of Fig. 4d), and this resorption occurred while some olivines were epitaxially overgrown by biotite, as evidenced by how an olivine phenocryst in Fig. 4(d) is less resorbed beneath protective biotite. In contrast, equally rounded ocelli are rather surrounded by what appears to be tangentially adhered biotites (Fig. 4e), suggesting that ocelli nucleated and rapidly expanded relatively late, after biotites had started crystallizing.

SEM element maps (Fig. B3) across a 3.1 mm²-large portion of a less easily defined matrix confirm that both olivine and kaersutite had stopped crystallizing, while augite, magnetite and biotite continued crystallizing together with accessory apatite needles, perovskite, minute rutile and even sulphides (Fig. 4f and -51_m in Table 2). While these more euhedral, early crystallizing phases constitute roughly half of this matrix area, the remaining half (Fig. 4g) is comprised of mostly analcime, some nepheline, minor calcite and accessory melilite, as late crystallizing interstitial phases (Table 2). Based on textural relationships between these more anhedral phases, it appears that analcime crystallized last, while it is more difficult to disclose crystallization sequences between the other three interstitial phases. There is no indication of the analcime having replaced another equally interstitial phase.

Sample 519751's conspicuously circular and transparent ocelli (Figs. 4e & B2c) differ from the sample's rounded olivines (e.g., Fig. 4d), by comprising more heterogeneous aggregates of mainly transparent minerals in among pale green and acicular aegerine crystals. While such ocelli – after first being regarded as amygdales –

Table 2. Bulk modal mineral proportions (incl. ocelli)

Samples	-51$_p$	-51$_m$	-54	-15
Rock type	HMD	HMD	CA	PN
Olivine	2.27			
Augite	42.31	36.23	15.79	5.81
Magnetite	6.65	6.05	6.71	2.55
Kaersutite	3.99			
Biotite	10.11	3.78	14.62	0.05
Sanidine	0.07	0.11		26.53
Apatite	1.39	2.16	5.05	0.61
Perovskite	1.27	1.98	2.14	
Rutile	0.29	0.01		1.43
Sulphide	0.03	0.45		0.10
Other	0.01	0.04		0.002
Early phases	*68.4*	*50.8*	*44.3*	*37.1*
Ocelli	*6.3*	*6.3*		*0.2*
Analcime	25.08	39.01	*44.94	48.76
Nepheline	5.09	7.92		
Carbonate	1.13	1.75	10.75	†14.16
Melilite	0.32	0.49		
Late phases	*31.6*	*49.2*	*55.7*	*62.9*
SUM	100	100	100	100

Including (p) phenocrysts, (m) matrix and ocelli, *22.5% Na-Ca-Si, and †8.1% dolomite.

were subsequently suspected to be immiscible carbonatite droplets, only two out of 64 SEM spot analyses on this thin section's ocelli (Fig. 4c) are calcitic and – in decreasing number of spot analyses within brackets – rather made up of silicic analcime (27), nepheline (14), augite-aegerine (8), leucite (2) and titanite (1). The first 27 spot analyses provide our most quantitative constraints on analcime (Na, $H_2O)[AlSi_2O_6]$, with half of its cations being silica, a quarter being aluminium, little less than a quarter being sodium, traces of calcium and totals between 84-89% allowing for additional water, not analysed for (cf., '29 analcimes' in Supplementary Data D).

More informative SEM backscatter and elemental maps (Figs. B3 & 5) further reveal that four ocelli are modally made up of 42–90% analcime, 0–43% nepheline and 0–2% sanidine, together with 4–6% augite-aegerine needles, 0–8% calcite and 0–5% melilite, as well as accessory apatite, magnetite and pyrite (Table 2); thereby replicating the interstitial phases found in the matrix of the same thin section (Fig. 4g). We find no indication of the analcime having crystallized from hydrothermal fluids, such as radiating zeolite or a concentrically zoned amygdale. Even if some augite-aegirine needles may represent partially incorporated microcrysts or even protrusions from a surrounding matrix, all phases inside these four ocelli (i.e., Fig. 5) – representing 0.96% of the thin section, compared to all ocelli constituting 6.3% – are included in Table 2's estimate of sample 519751's modal mineral proportions. The estimate excludes biotite; however, since these crystals appear to have adhered onto the outer surface of such melt droplets (Fig. B3), rather than having crystallized from it and draping the inside of droplet walls.

Textural relationships inside the studied ocelli improve constraints on the crystallization sequence among late-stage

phases, with more euhedral augite-aegerine and magnetite → (crystallizing before) subhedral nepheline and sanidine → anhedral melilite and calcite → surrounding analcime. The melilite-rich ocellus section in Fig. 5(a) provides the best evidence of melilite crystallizing epitaxially along the walls of this ocelli and – in the absence of nepheline and sanidine – possibly even together with augite-aegerine. Rather than forming a second stage of immiscible droplets inside these ocelli, however, calcite more often appears to also have crystallized against ocelli walls or pre-existing nepheline (e.g., in the most calcitic ocellus section in Fig. 5b). This is substantiated by the most intriguing ocellus section in Fig. 5(c), which not only includes all mentioned phases but also an unconstrained envelope that is more calcic and less sodic than analcime and incorporates a high concentration of both melilite and calcite. This enigmatic (hybrid?) zone drapes nephelines and sanidines and is in turn draped by analcime, suggesting that while more calcic phases grew onto pre-existing nephelines and sanidines, hydrous analcime was the last to crystallize inside this ocellus. Again, there is no indication of the analcime having replaced another phase and must thereby have crystallized as a primary magmatic – albeit late-stage and fluid-rich – phase.

3.c. Damtjernite-hosted autoliths

Two coarse-grained nodules, from inside a proximal dyke (519714; Fig. B4), mainly comprise of more euhedral and likely cumulus augites (no olivine) and subhedral magnetites, surrounded by intercumulus kaersutite (no biotite). This assemblage resembles that of phenocrysts inside evolved damtjernites but where these nodules more clearly show how kaersutite crystallized after augite and magnetite. The nodules also contain additional larger abundances of euhedral and thereby early crystallizing apatites, as well as isotropic fluorites, which are not observed as phenocrysts within the two studied damtjernite dykes. SEM spot analyses further reveal how these nodules contain cumulus augites (Di$_{50-47}$), kaersutites (Mg# ~58-34) and magnetites, which are all only slightly more evolved than analysed damtjernitic phenocrysts (Fig. B9). These nodules arguably provide the most direct information about cumulates within a central magma chamber and could potentially have accumulated from magmas like their damtjernitic host dyke.

3.d. Carbonaceous alnöites

Two selected samples serve to illustrate the petrography of typically more aphyric, thinner and relatively scarce alnöite intrusions (Fig. 2e). Because of their fine-grained nature and presence of rarely more than micro-phenocrysts, it is difficult to identify minerals under a microscope. Reconnaissance SEM spot analyses only reveal that both samples include augite, apatite, magnetite and some biotite, typically as slightly larger crystals. Relatively low-resolution SEM elemental maps for a more altered 519749, with partly amphibolitized augite micro-phenocrysts, did not allow all phases to be fully traced. Nevertheless, the resulting phase map in Fig. B5(b) still reveals that this thin section's dominating paler patches are richer in feldspathoids, apatites and magnetites, while slightly darker zones in between these patches are much more carbonaceous (including both calcite and ankerite), devoid of aluminium and hosting rutile rather than magnetite. It is tempting to interpret these different zones as an incipient separation into more feldspathoidal and carbonaceous magma parts, which could have segregated after augite started crystallizing, judging from how augite crystals appear more evenly dispersed across both zones.
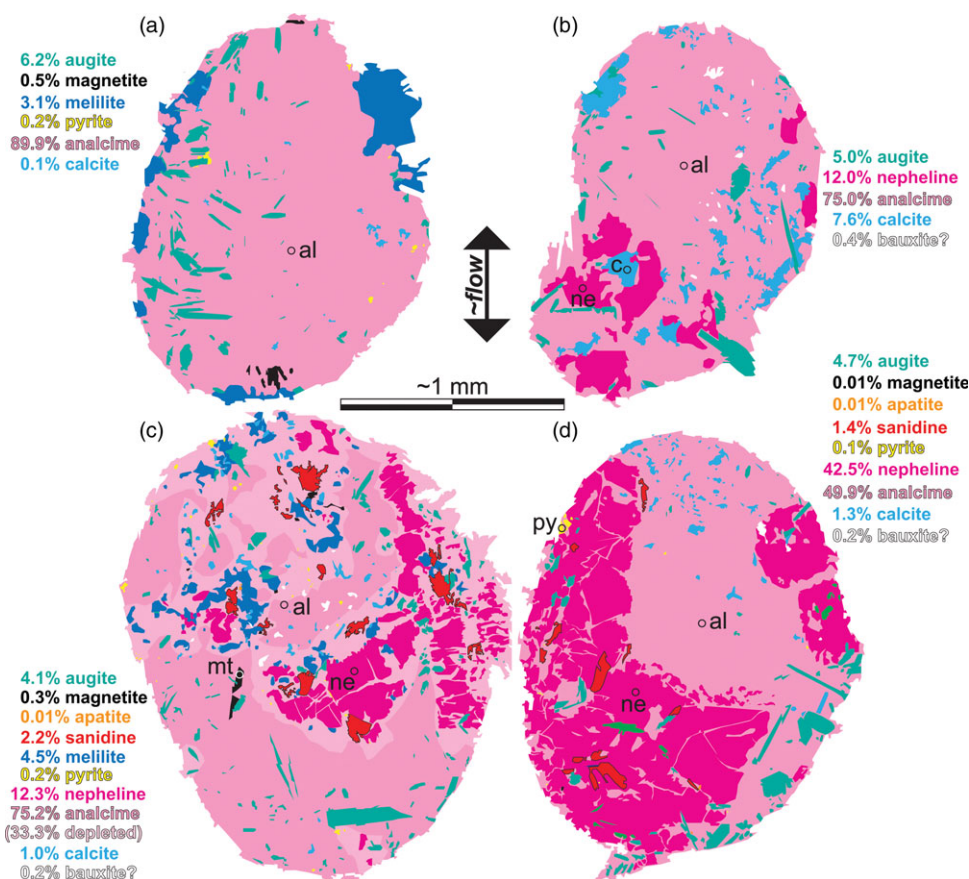
Figure 5. (Colour online) Phase maps of four ocelli, traced from SEM electronic backscatter and elemental maps in Fig. B3. Labelled circles locate SEM spot analyses for analcime (al) nepheline (ne), calcite (c), magnetite (mt) and pyrite (py). 'depleted' refers to a zone between nepheline and analcime with lower Na and higher Ca, inside which most calcite and melilite also resides. Otherwise, as in Fig. 4.

A slightly coarser-grained and fresher 519754 (Figs. B6 & 6) does not exhibit as much zoning as 519749 but a more evenly aphyric to slightly augite-microphyric texture. A complete SEM elemental mapping of a 9.9 mm^2-large area of this thin section shows that 519754 is made up of early crystallizing augite, biotite, magnetite, apatite and perovskite (Fig. 6b). Even if this mineral assemblage resembles that of damtjernites (Fig. 4f), the alnöite matrix in Fig. 6(b) hosts less augite and a greater proportion of apatite and biotite compared with the matrix of the porphyritic HMD (Fig. 4f) and, most importantly, a smaller proportion of early crystallizing phases (44.3%) compared to either the HMD's matrix (50.8% for -51$_m$ in Table 2) or the entire thin section, including phenocrysts (68.4% for -51$_p$ in Table 2).

Like within the damtjernites, interstitial phases of sample 519754 are also made up of mostly analcime, but also an equal proportion of unidentified more calcic and less sodic Ca+Na+Si phase that – much like an ocelli's 'hybrid' zone in Fig. 5(c) – typically is located in between the analcime and apparently earlier crystallizing calcite (Fig. 6b). All these late crystallizing interstitial phases constitute a significantly larger proportion within this alnöite, compared to the HMD (55.6% vs 31.7% of interstitial phases, respectively, in Table 3).

3.e. Phonolitic nephelinites

Samples from an inward dipping sheet (519711) and a radiating dyke (519715), serve to illustrate the petrography of typically more aphyric and thinner nephelinite intrusions, emplaced closest to the magmatic centre (Fig. 2g). The inclined sheet (519711) exhibits an overall pale-spotted texture (Fig. B7a) that incomplete SEM

Table 3. Interstitial analcime:carbonate proportions

Sample	Portion	Slide %	Al:CO$_3$
HMD (-51)	Matrix	25.4	96:4
	Ocelli	6.3	98:2
	Total	31.7	96:4
CA (-54)	Total	55.6	*81:19
PN (-15)	Ocelli+vein	2.3	99:1
	Grey blebs	4.3	52:48
	Rest	55.3	93:7
	Total	61.9	91:9

* 40% analcime and 41% 'hybrid' Ca+Na+Si phase.

mapping (Fig. B7b) reveals to represent (K, Si)-rich spots, surrounded by (Na, Ca)-rich darker zones. Among more euhedral crystals that are large enough to be identified and mapped in Fig. B7(b), augite and apatite needles, as well as a remarkably large abundance of euhedral and equigranular perovskites, appear to be dispersed relatively evenly throughout both matrix zones, suggesting that these crystallized before the (K, Si)- and (Na, Ca)-rich portions segregated from each other. Preferentially SEM spot analysed sanidine micro-phenocrysts on the other hand reside exclusively inside (K, Si)-blebs, while magnetite, pyrite and some euhedral analcime crystals appear restricted inside intervening (Na, Ca)-zones, together with euhedral nephelines. Thus, it appears that 519711's sanidines and nephelines started crystallizing after earlier augites, magnetites, apatites and perovskites and
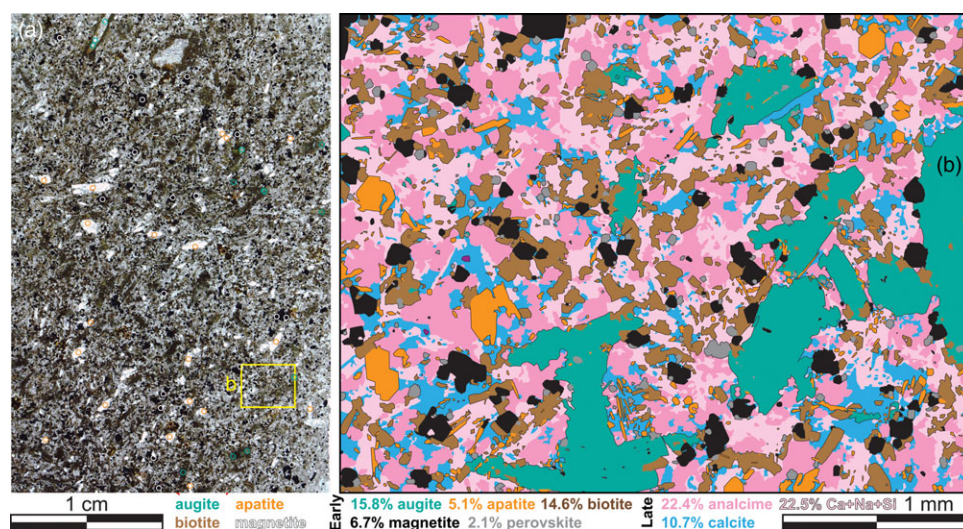
Figure 6. (Colour online) The most carbonaceous of two alnöite thin sections, 519754. (a) Thin section scan with more obvious apatite and augite micro-phenocrysts and even smaller magnetites, surrounded by biotites. Colour-coded circles locate SEM spot analyses (Fig. B9). (b) A 9.9 mm²-large phase map of matrix portion located in (a), based on SEM electronic backscatter and elemental maps in Fig. B5. Otherwise, as in Fig. 4.

thereby left behind an interstitial melt inside the (Na, Ca)-rich darker zones that subsequently segregated into more analcime-rich and carbonaceous parts (cf., Fig. B7b).

The crystallization sequence for the above nephelinite sheet sample 519711 is more convincingly supported by nephelinite dyke sample 519715 (Fig. 7), which is sufficiently coarse to allow all its phases to be identified from SEM elemental maps (Fig. B8). While this thin section is not as distinctly spotted as 519711, it still contains ~5.7% of more irregular greyish patches, in among paler areas, separated by darker transition zones (Fig. 7a). The 6.6 mm²-large SEM element maps in Fig. 7(c-d) reveals that one such grey patch is dominated by carbonates, while its paler surroundings incorporate more analcime. Both interstitial phases constitute 61.6% of this map and reside inside an open network of early crystallizing phases, dominated by sanidines throughout but without any augites residing inside the carbonated patch (Fig. 7c). Magnetite and rutile are the most abundant accessory phases, as opposed to mainly pyrite in 519711, with rutile being more common among carbonates. Little – if any – nepheline occur together with mainly analcime, while the carbonaceous patch comprises of more dolomite than calcite.

The thin section of sample 519715 (Fig. 7a) also contains a thin vein and isolated paler spots, including a larger ocellus that is linked to that vein. A segment of this vein, mapped in Fig. 7(d), comprises 89% analcime and 11% calcite, resembling proportions calculated for the entire thin section (90% vs 10%, respectively), as detailed in Section C2 and listed in Table 3. In comparison, the ocellus (Fig. 7b) is almost entirely made up of analcime (99%), with only ~1% calcite (Table 3), after excluding early crystallizing acicular sanidines that likely protrude from the surrounding matrix and accessory pyrites and magnetites that line the walls of the ocellus. Together with analcime-dominated ocelli in our damtjernite sample (Fig. 6), this suggests that analcime rest melts more readily form ocelli than carbonaceous rest melts.

3.f. Summary of key petrographic results

Through various textural relationships, it may be generalized that the crystallization sequence is olivine → augite → magnetite → kaersutite → biotite (during resorption of olivine and kaersutite) → apatite/fluorite/perovskite/rutile/pyrite (more difficult to discriminate between these five phases) → sanidine → nepheline → melilite → calcic-, magnesian- and/or ferrous carbonates → analcime. Through phenocryst and SEM phase maps, as well as discriminations between predominantly analcime-bearing ocelli and veins versus more carbonaceous zones, it is possible to quantify phase proportions for all four rock types (Tables 1–2). The ubiquitous presence of analcime, together with carbonates, across all rock types suggests both a cogenetic relationship and that all phases are igneous, rather than secondary. This view is supported by how proportions of early crystallizing phases diminish, while proportions of interstitial late phases increase, and how ratios between analcime and carbonates, as dominating interstitial phases, differ between CA and PN (Table 3), for example, induced by fractional crystallization and late-stage (± immiscible) segregations within interstitial rest melts.

4. Bulk rock geochemistry

The map in Fig. 2(e) includes 22 sample locations across its north-western parts, which were collected by others (working for GEUS) and reported by Hansen (K Hansen, unpub. MSc thesis, Univ. Copenhagen, 1979, 1980, 1981, 1984), Larsen & Rex (1992) and Larsen *et al.* (2009). These 22 samples appear to have been collected along potentially as few as 11 different dykes, as occasionally supported by similar bulk rock compositions (cf., sample symbols in Fig. 2e) and/or similar dyke thicknesses (cf., Fig. C1a). Inside the three sub-areas N, C and S (framed in Fig. 2e), an additional 27 samples were collected in 2010 by the first author from 20 different radiating dykes and five different centrally inclined sheets. While older GEUS samples were processed and analysed as detailed in the above references, new samples were processed and analysed for bulk rock geochemistry and mineral chemistry at the Central Analytical Facility of Stellenbosch University (Supplement A), and all 49 new and published sample analyses are presented in Supplement D. Only 18 of the older samples, however, provide a wider suite of trace elements, reducing the total number with more complete datasets to 45 samples from 39 different localities and 35 independent dykes (26) and cone sheets (9).

4.a. Geochemical classification

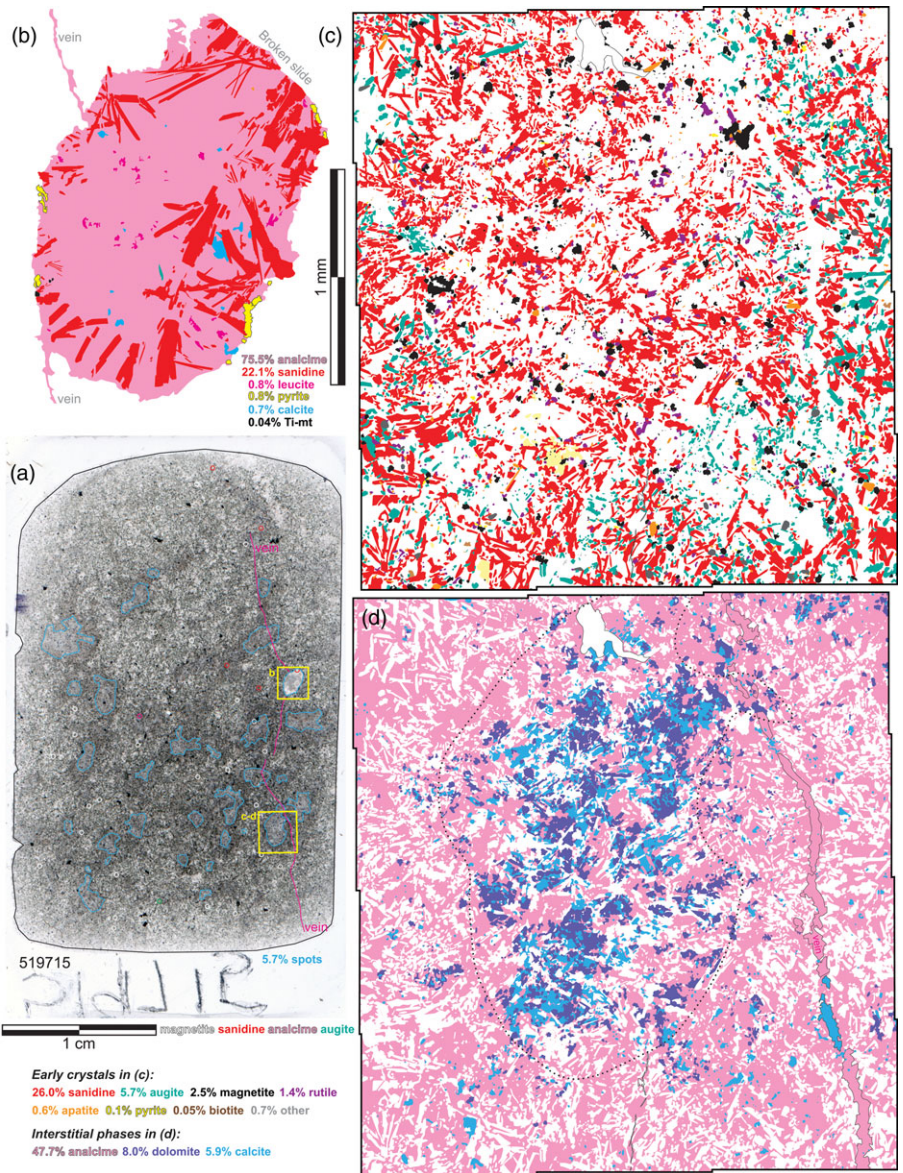Geochemically, FHI samples plot along the more aluminous lamprophyre base of Bergman's (1987) ternary classification

Figure 7. (Colour online) Sample 519715 from a proximal nephelinite dyke. (a) Scanned thin section with few micro-phenocrysts of mainly opaque magnetites, a solitary apatite and mostly analcime-bearing paler patches, including one distinct ocellus, set in a fine-grained matrix with 6.3% greyish patches. Colour-coded circles locate SEM spot analyses (Fig. B9). Phase maps, based on SEM elemental maps in Fig. B8, for (b) ocellus, as well as (c) early and (d) late crystallizing phases within a 6.6 mm²-large matrix area, dominated by a central grey patch. Otherwise, as in Fig. 4.
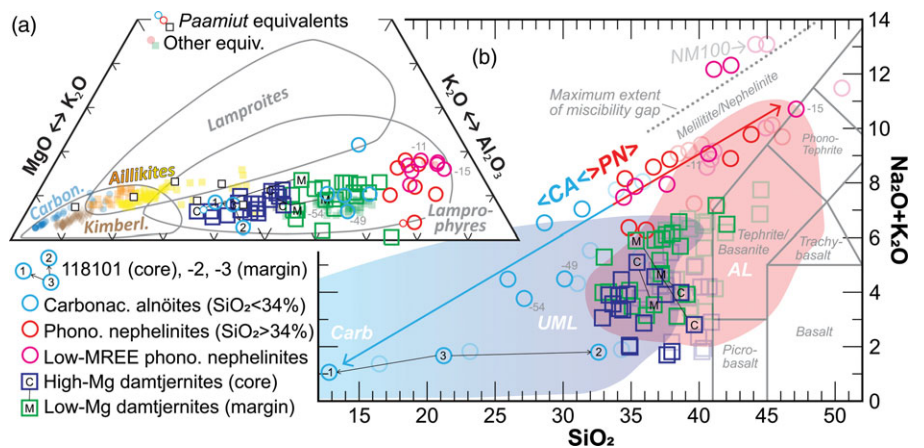

Figure 8. (Colour online) Classification diagrams by (a) Bergman (1987) and (b) Le Maitre (2002), where this paper's samples group into either high- or low-Mg damtjernites (HMD and LMD, respectively) and an associated suite of carbonaceous alnöites (CA) to phonolitic nephelinites (PN). Subdued sample symbols in (b) exclude volatiles and are normalized to 100%. According to Rock (1987), blue UML-field = ultramafic lamprophyres and red AL-field = alkali lamprophyres. Carb = Carbonatite.
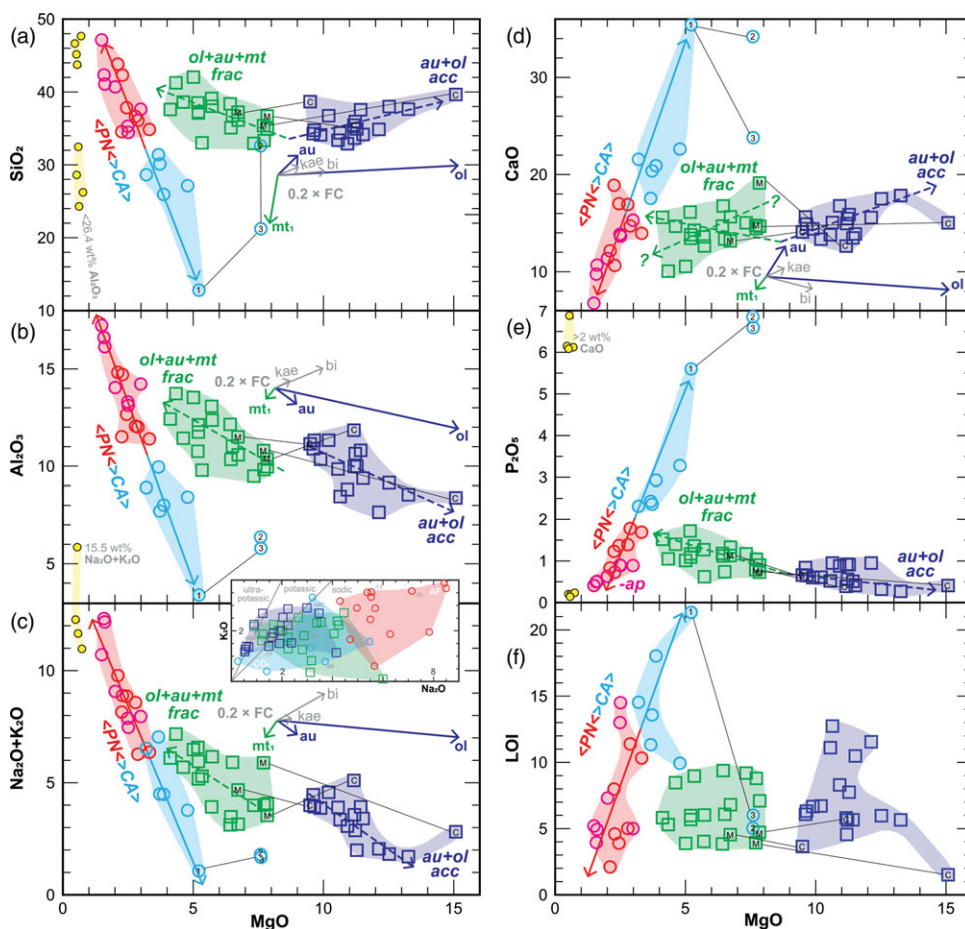
Figure 9. (Colour online) Six major oxide variation diagrams with MgO as differentiation indices. (a-c) 'Alkali feldspathic' oxides with negative sloping CA-PN trends. Insert plots K_2O against Na_2O. (d-f) 'Carbonatitic' oxides and loss of ignition (LOI) with opposite positively sloping CA-PN trends. Yellow-filled circles represent concentrations in the four different ocelli cross sections in Fig. 5, calculated from mapped phase proportions and their stoichiometric compositions. Symbols and annotations as in Fig. 8.

diagram, separate from more magnesian kimberlites, aillikites and associated (often magnesian) carbonatites, as well as more potassic lamproites (Fig. 8a). FHI samples further plot across the silica-poorer foidite side of a Total Alkali vs Silica (TAS) diagram (Fig. 8b), after preferably not eliminating loss on ignitions (LOIs) and normalizing major elements to 100%, because these rocks may have substantial igneous CO_2 components. Fig. 8(b) also shows how FHI's damtjernites plot where Rock's (1987) compositional ranges by ultramafic and alkali lamprophyres overlap (UML and AL, respectively, in Fig. 8b). In contrast, more alkali CA to PN mostly plot along a rough CA-PN array above these damtjernites, which extends from the carbonatite end of Rock's (1987) UML field, across the TAS diagram's foidite field and into the more alkali and silica-rich extent of Rock's (1987) AL field, to almost plot as phonolites.

4.b. Damtjernites

Twelve selected variation diagrams in Figs. 9–10, with MgO as a common differentiation index, illustrate how HMDs and LMDs define two distinct geochemical groups, with more or less than ~8.5 wt% MgO, respectively. Among these plots, Sc (Fig. 10e) is the only element that exhibits a single coherent, albeit scattered, linear trend, which even extends into the alnöite–nephelinite suite. The other eight plots exhibit more or less elbowed HMD and LMD trends, where elbows for SiO_2, CaO, P_2O_5, MnO and rare earth elements (REEs) (Figs. 9a, e & 10c, f) are convex upward and Fe_2O_3, TiO_2 and Co (Fig. 10a-b, d) are convex downward. Despite

some being poorly defined, the commonly discordant trends for HMDs and LMDs can still be reversely modelled separately, as detailed in Supplement C and briefly summarized in the following text for a maximum of three co-fractionating phases.

Our reversed geochemical modelling uses SEM spot analysed HMD phenocryst compositions (Fig. B9), firstly, for earliest crystallizing olivines, augites and magnetites, which were all seen to accumulate inside the more primitive and panidiomorphic dyke core sample 519768C (Fig. B1f). These phases define irregular phase triangles in Fig. C2, through which manually fitted HMD and LMD trend lines consistently pass. The ways that trends intersect these irregular phase triangles are transposed onto a more quantifiable ternary diagram (Fig. 10g), where six HMD trends are consistent with the fractionation/accumulation of between 70–88% augite, 5–24% olivine and 0–22% magnetite, while six intersecting LMD trends require more magnetite (29–45%), together with roughly similar proportions of olivine (4–28%) and less augite (33–68%), likely having fractionated from these more aphyric samples. These results may be simplified as HMD trends being controlled by mostly augite, including some olivine; whereas, LMD trends are controlled by additional magnetite. A similar dominance of augite fractionation also controlled the diversification of lamprophyric magmas within the Kola Peninsular (Nosova *et al.* 2021a).

Since biotites appear to replace resorbed olivines within the more evolved dyke core sample 519751 (cf., Fig. 4d), the same trends are reversely re-modelled through augite–magnetite–biotite phase triangles (Fig. C2) but result in roughly similar proportions
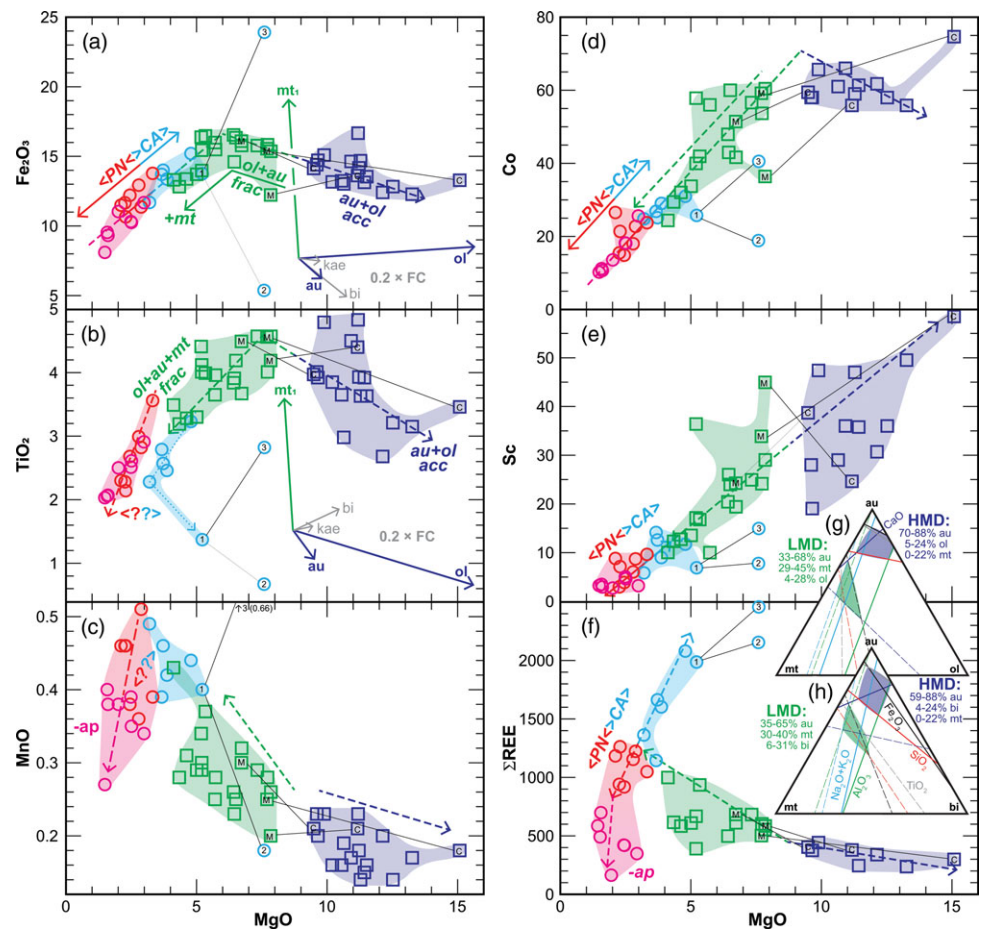
Figure 10. (Colour online) Three major oxide (a-c) and three trace element (d-f) variation diagrams with MgO as differentiation indices. (g-h) Reverse modelling results for HMD and LMD trends, derived from Figs. C2 & C3, respectively, where every intersection collectively delineates a colour-coded area that quantifies the range of possible fractionating/accumulating phenocryst assemblages, listed next to these. Symbols and annotations as in Fig. 8.

(Fig. 10h). Thus, suggesting that augite is the most important phase for both HMDs and LMDs, magnetite becomes important for LMDs, while it matters less what type of additional mafic phase (whether early crystallizing olivine, late crystallizing biotite, intermediate kaersutite or any mixture of these) fractionated, or accumulated, together with these. The question just becomes how the above-modelled assemblages are either fractionated or accumulated in order to form both HMDs and LMDs? In Section 5(a), the following three fractionation models will be discussed: (1) elbowed HMD and LMD trends simply representing liquid lines of descent from a more magnesian parent; (2) *in situ* dyke flow segregation, where magnetite is mysteriously decoupled from accumulating into dyke cores; and (3) dykes tapping a fractionated magma chamber top, occasionally followed by the entrainment of an unconsolidated mafic cumulate mush (without denser magnetites).

In addition to having discordantly elbowed trends, HMD and LMD trends defined by Al₂O₃ (Fig. 9b) and total alkalis (Fig. 9c) are rather offset from, than connected to, each other, with HMD samples having overall more elevated concentrations than LMD samples. Since analcime-rich ocelli are particularly sodic and aluminous (yellow-filled circles in Figs. 9–10 & C1), it is reasonable to suspect that these offsets reflect an accumulation of such ocelli into HMD samples. Since three dykes have both porphyritic HMD cores and almost aphyric LMD margins, it may be further speculated that ocelli flow segregated from dyke margins and more readily accumulated into HMD dyke cores. Such an interpretation

is supported by a higher proportion of ocelli within the most porphyritic core sample 519751 (6.3%), compared to a less porphyritic core sample 519750C (0.8%) from the same dyke (Table B1 and Fig. B2).

4.c. T-trends by more evolved rocks

More evolved alnöites and nephelinites define trends that occasionally form an extension of LMD trends (e.g., Fig. 10a-e), as expected if these simply formed through continued biotite, augite and magnetite fractionation from an LMD parent. In the remaining 8 of 13 selected variation diagrams in Figs. 8(b) and 9–10, however, alnöite–nephelinite trends define discordant T-junctions to LMD trend extrapolations, much like how one would expect liquid immiscibility to split towards carbonatitic and feldspathoidal end members. Two types of T-junctions are recognized, where (1) nephelinites become more enriched in SiO₂, Al₂O₃ and total alkalis (Fig. 9a-c) and (2) alnöites become more enriched in CaO, MgO, P₂O₅ and REEs (PN-CA in Figs. 9d-e & 10f). These oxides and elements are either the building blocks of, or highly compatible with, interstitial analcime or carbonates, in total constituting 62 and 56 modal-%, respectively, of nephelinite sample 519715 and alnöite sample 519754 (Table 2). Together with how ratios vary between analcite and carbonates (Table 3) and their bleb-like mingling amongst each other (Figs. B5a, 7a & B7a), it is therefore tempting to relate these alnöite–nephelinite trends to segregations of such interstitial analcime and carbonatite rest melts.
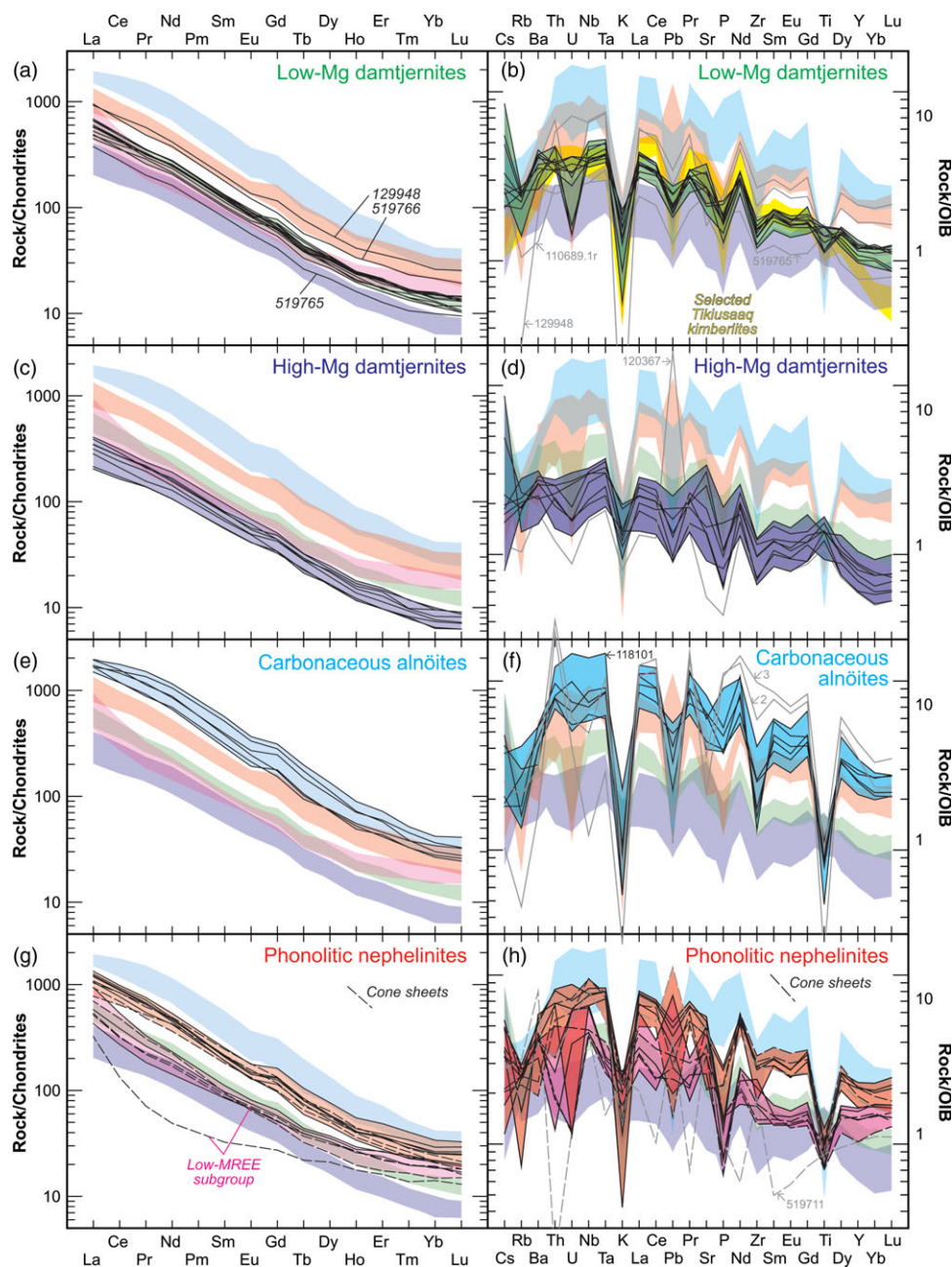
Figure 11. (Colour online) Chondrite-normalized rare earth element (REE) and OIB-normalized incompatible element patterns (Sun & McDonough, 1989). (a-b) LMDs (green), compared to selected Tikiusaaq kimberlites (yellow) from Tappe *et al.* (2017a). (c-d) HMDs (purple). (e-f) Carbonaceous alnöites (cyan). (g-h) Phonolitic nephelinites (red), where a subgroup (magenta) has relatively low (concave-up) MREE patterns.

One observation that could question such late-stage analcime–carbonatite segregation is that extrapolations of LMD trends by SiO_2 and Al_2O_3 (Fig. 9a-b) do not consistently intersect where more evolved T-trends separate into either nephelinites or alnöites but intersect more nephelinitic compositions. As will be discussed in Section 5(c), this likely reflects superimposed SiO_2 and Al_2O_3 loss as magmas transitioned from an evolved LMD parent and into the alnöite–nephelinite segregation, for example, through sanidine fractionation. This sanidine fractionation is consistent with how nephelinites are more sodic than other rock types, as shown by the Na_2O versus K_2O insert in Fig. 9(c). Finally, one may also note that it is difficult to resolve which of the two segregated end members is more evolved than the other, where alnöites are more magnesian, and thereby arguably more primitive, yet on the other hand also – as illustrated by REEs (Fig. 10f) – more enriched in incompatible elements than nephelinites, typical for more evolved magmas.

4.d. Incompatible element signatures

Both REEs and additional incompatible elements (left and right columns of Fig. 11, respectively) display remarkably parallel patterns, which for our four main rock types are displaced, relative to each other, so that (1) HMDs (Fig. 11a-b) have overall lowest concentrations, as expected for more primitive rocks, including cumulates that further expelled intercumulus melts, while (2) LMDs (Fig. 11c-d) have higher concentration, as expected after fractionation of phenocrysts with relatively low concentrations. These LMD patterns are, nevertheless, lower than even more evolved nephelinites and alnöites, where (3) CAs (Fig. 11e-f) have the overall highest incompatible element concentrations (Fig. 11h), while (4) nephelinite patterns have concentrations that are intermediate to alnöites and LMDs. PN further include a subgroup with particularly low Middle Rare Earth Element (MREE) concentrations (convex-down

REE patterns in Fig. 11g) that partly overlap LMD patterns and may have experienced apatite fractionation. Apart from this low-MREE nephelinite sub-group, all samples from all four rock types within the FHI complex – as mentioned – share conspicuously similar incompatible element patterns (i.e., signatures), supporting a cogenetic relationship.

Incompatible element patterns are for most parts more enriched than Ocean Island Basalts (OIB), thought to be derived from an enriched mantle plume. Patterns are not particularly more enriched in large ion lithophile elements (LILE), compared to high field strength elements (HFSE) and do not possess negative Nb-Ta anomalies, consistent with parents derived from a mantle source that has never been metasomatized within a supra-subduction zone. Instead, patterns are noted for their consistently negative K-spikes, which also become more pronounced upon differentiation and must thereby partly relate to some phlogopite/biotite fractionation from damtjernitic magmas, as well as sanidine from nephelinites. Likewise, progressively more pronounced negative Ti-anomalies for more evolved samples support notions from Fig. 10(a-b) and petrographical observations that indicate a relatively early onset of magnetite fractionation, shortly after olivine and augite. Furthermore, the proposed apatite fractionation from low-MREE nephelinites (pink in Fig. 11h) is supported by their more negative P-spikes. Since this P and MREE depletion appears coupled with less negative K-anomalies, compared to other nephelinites, low-MREE nephelinites likely experienced less fractionation or even accumulation of sanidines.

Despite some fractionation of K-, P- and Ti-rich phases, the most parental damtjernite patterns still exhibit negative K-anomalies, as well as less distinct P-anomalies, which could have been inherited from the mantle source. Such an interpretation is substantiated by how roughly coeval kimberlites from a nearby Mesozoic Tikiussaq complex (cf., yellow background in Fig. 11b) – with the exception of having much lower Heavy Rare Earth Element (HREE) concentration, likely related to deeper segregations from their more garnet-rich mantle source – share conspicuously similar patterns with FHI's LMDs and are regarded as primary magmas (Tappe et al. 2017a). Consequently, this not only argues for LMDs having close to primary compositions but also records a similar mantle source type for both complexes, even if Tiklussaq's kimberlitic source was deeper than that of FHI's damtjernites.

5. Discussions

Based solely on how bulk rock geochemical analyses plot in variation diagrams (Fig. 9–10), it could be tempting to discriminate FHI's more primitive damtjernites from more evolved nephelinites and alnöites as a pair of independent magma suites. A cogenetic relationship is, however, suggested by their converging intrusive field relationships (Figs. 1–2), parallel incompatible element patterns (Fig. 11), as well as how all of FHI's rock types conspicuously share petrographic characters, including interstitial analcime and carbonate phases that increased in proportions during differentiation (Table 3). Other studies likewise link similar rock types with each other (e.g., Nosova et al., 2021). Before discussing how all rock types may be cogenetic and only differ due to a sequence of different magma diversification processes, however, we first need to constrain a potential common parent.

5.a. A common parental-primary magma

A parental magma may simply be defined as the most magnesian sample 519768C, with a Mg# of 71, 217 ppm Ni, 678 ppm Cr and

olivines (Fo$_{80-88}$; Fig. 9a) that are almost mantle-like (Fo$_{88-92}$; e.g., Veter et al. 2017; Nosova et al. 2018). However, considering that the sample's panidiomorphic texture (Fig. 5b) and collection from a potentially flow-segregated porphyritic dyke core (Fig. 4d), its melt component is expected to be less primitive than its bulk composition. Since all personally sampled aphyric margins and more porphyritic cores consistently plot as LMDs and HMDs, respectively, it is furthermore tempting to interpret all other LMD and HMD samples as, likewise, either more differentiated dyke margins and cumulative cores, respectively. If all HMDs are cumulates, the parent would rather be intermediate to HMD and LMD subgroups. A more intermediate parent with ~8.5 mass-% MgO is further supported by how LMDs share similar incompatible element patterns as Tikiusaaq's primary calcite kimberlites (Fig. 11b), apart from HREEs in the latter being lowered by residual garnet.

Since negative K, P, Zr and Ti spikes of primary Tikiusaaq's calcite kimberlites cannot have been induced by later phlogopite, apatite, zircon and ilmenite fractionation, respectively, remaining anomalies must have been inherited from such residual phases within, for example, a MARID metasomatized sub-continental lithospheric mantle (SCLM) source (cf., Tappe et al. 2008, 2011), proposed for Tikiusaaq (Tappe et al. 2017a), including phlogopitic mica (M) and kaersutitic amphibole (A), together with rutile (R), ilmenite (I) and diopside (D). Shared geochemical signatures further argue that existing isotopic constraints on the petrogenesis of Tikiusaaq magmas likely also apply to FHI's damtjernitic parent. Having hereby – to the best of our ability – constrained a potential common parent, we may shift focus to its further diversification, starting with damtjernites (Section 5b) and then moving on to a more evolved alnöite–nephelinite suite (Section 5c).

5.b. Damtjernite diversification

Given that mainly augite, together with some other mafic phase (olivine, kaersutite and/or biotite), controlled HMD trends and additional magnetite controlled LMD trends (Fig. 10g-h), three different diversification processes are envisaged. The simplest interpretation is that these phase assemblages successively fractionated from a more magnesian parent, inside a central magma chamber and during contemporaneous dyke injections of progressively more evolved differentiates. This model faulters, however, on thicker dykes having both porphyritic HMD cores and less phyric LMD margins. Instead, speculations into how more porphyritic dyke cores formed through in situ flow segregation of phenocrysts from distinctly less porphyritic dyke margins are supported by (1) 519768C's panidio-morphic texture, comprised of mostly augites, fewer olivines and sporadic magnetite micro-phenocrysts, compared to that dyke's margins (Fig. B1e-f), (2) overall phenocryst size differences between two nearby core samples (519750C & 519751 in Figs. 4b-c & B2e-f) from the same dyke, reflecting phenocrysts growth during dyke emplacement, and (3) the bulk rock compositions of three dyke core–margin sample pairs, consistently plotting as HMDs and LMDs, respectively (Figs. 9–10). Consequently, suggesting that all other HMD samples were, likewise, collected from porphyritic dyke cores, while LMDs exist as both aphyric margins and aphyric dykes without porphyritic cores. If so, then the diversification of damtjernites could mainly have been controlled by in situ flow segregation.

On closer scrutiny, however, geochemical plots of Hansen's (K Hansen, unpub. MSc thesis, Univ. Copenhagen, 1979) core–margin pair (110689.2_c & -1_r) often trends oblique to the other two core–margin pairs of this study and neither of the three sample pairs fully
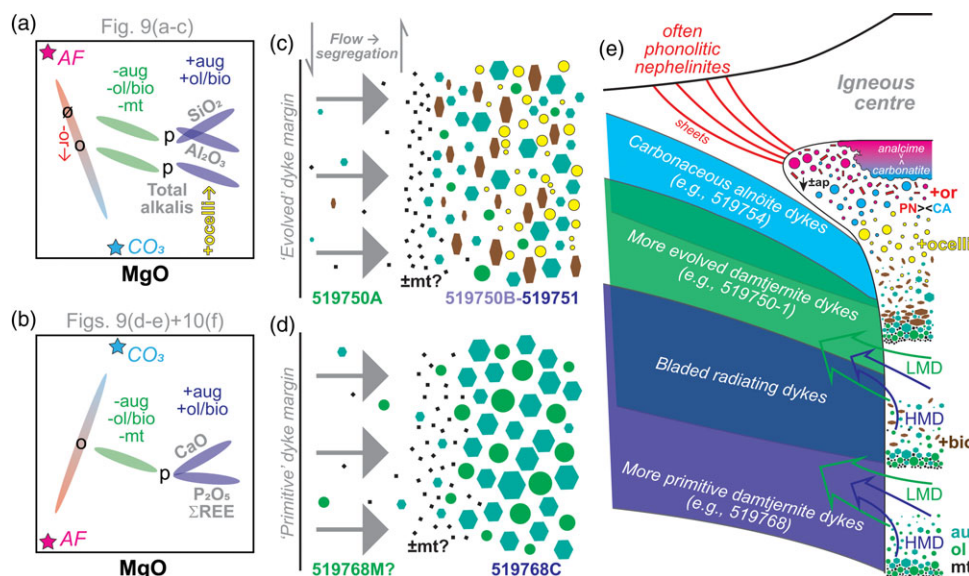
Figure 12. (Colour online) Damtjernite diversification. Sketch diagrams compiling (a) Fig. 9(a-c) and (b) Figs. 10(d-e) and 11(f), where p = parental magma to both HMDs (purple) and LMDs (green). o = more differentiation 'parent' to CA-PN suite, with ø deviating from this. Two dyke half-widths exemplify how (c) a more evolved (519750A, -B & -51, modified from Fig. B2a-c) and (d) primitive magma (519768 & -C, modified from Fig. B1e-f), experienced flow segregation (grey arrows), where densest and smaller magnetites were less affected than least dense and larger ocelli. (e) Central magma chamber, from which bladed dykes first tapped differentiated upper parts, followed by partially accumulated crystal mushes, during three stages in its evolution, accumulating (from bottom to top) early olivine, augite and magnetite, later additional biotite/kaersutite, and eventually also ocelli, orthoclase (or) and apatite (ap). Yellow ocelli can also represent more mixed rest melt segregations, eventually segregating into analcimic (magenta) and carbonatitic (cyan) ocelli and ultimately aggregating into upper pockets of more buoyant analcime overlying denser carbonatites.

conform to the trends that were reversely modelled in Fig. C1. It is also problematic how the bulk rock geochemistry of damtjernitic samples does not collectively combine into coherent linear trends (only in Figs. 10e & 11e), without elbows, as expected for wholesale flow segregation of bulk phase assemblages. As schematically summarized by Fig. 12(a-b), damtjernites instead define two separate, more or less obvious but often discordant trends (Figs. 10a-d & 11a-d,f), which are further offset for Al_2O_3 and total alkalis (Fig. 9b-c). Thus, if these trends were produced through *in situ* flow segregation, HMD dyke cores must have accumulated mainly augite, together with some other mafic phase, while LMD margins fractionated additional magnetite. Such apparent decoupling by magnetite poses the biggest issue with the *in situ* flow segregation model and needs to be addressed.

With grain dispersive pressures thought to be the underlying force behind flow segregation during laminar magma flow inside dykes (Komar, 1972), such a force is further expected to get exponentially stronger towards dyke margins and have a greater impact on larger and less dense phenocrysts and ocelli (Fig. 12c-d). Thus, in order to explain the required flow segregation, more margin-proximal grain dispersive pressures would have had to be strong enough to remove mafic phenocrysts and magnetite micro-phenocrysts from dyke margins, while selectively transporting larger and less dense phenocrysts and eventually also ocelli farther into dyke cores. If it is more difficult for such pressures to transport denser and smaller magnetite micro-phenocrysts from LMD margins, magnetites could have accumulated between dyke margins and cores (Fig. 12c-d) that were never sampled and thereby generate a biased dataset of apparent magnetite decoupling during *in situ* flow segregation. Such a differential flow segregation force is also consistent with relatively large, lower-density and analcime-dominated ocelli being transported farthest into accumulating dyke cores (cf., '+ocelli→' in Fig. 12a-b) and thereby

explains why HMDs are overall more enriched in Al_2O_3 and total alkalis, compared to LMD dyke margins. While only denser sampling profiles across dykes with both aphyric margins and porphyritic cores (e.g., Barron, 1996) and numerical modelling may test the above differential flow segregation hypothesis, however, there also exists a third explanation, offering a more realistic explanation for the enigmatic magnetite decoupling.

In order to solve the *in situ* flow segregation model's problematic decoupling of magnetite, we propose that aphyric thinner dykes and dyke margins could have tapped a more differentiated LMD portion of a central magma source, which during extended laminar filling of thicker dykes could be followed by an unconsolidated HMD cumulate mush (Fig. 12e). Denser magnetite phenocrysts would in such a magma chamber source tend to accumulate faster, deeper and more out of reach from tapping dykes. Such retention of accumulated magnetites inside igneous centres is, furthermore, consistent with the characteristic positive aeromagnetic anomalies of central carbonatite complexes (e.g., Fig. 2a-e). During the evolution of such a central magma chamber source, repeated tapping could – as illustrated by Fig. 12(e) – have first fed more primitive damtjernite dykes (like 519768), which only accumulated anhydrous olivines and augites (Fig. B1), while later dyke injections from a more evolved magma chamber (like 519750-1) entrained cumulate mushes with hydrous kaersutite and biotite (Figs. B2 & 4). As an alternative more applicable to low-volume alkali plumbing systems, the tapping of numerous independent magma pockets that evolved through roughly similar fractional crystallization processes could help explain the scattered geochemical trends in Figs. 9–10 & C2-3. Still, the main advantage of either of these two source-tapping models, compared to *in situ* flow segregation, lies in denser magnetites being able to accumulate more deeply into a magma chamber and thereby avoid getting drawn into HMD dyke cores, while still gravitationally fractionating from a more differentiated
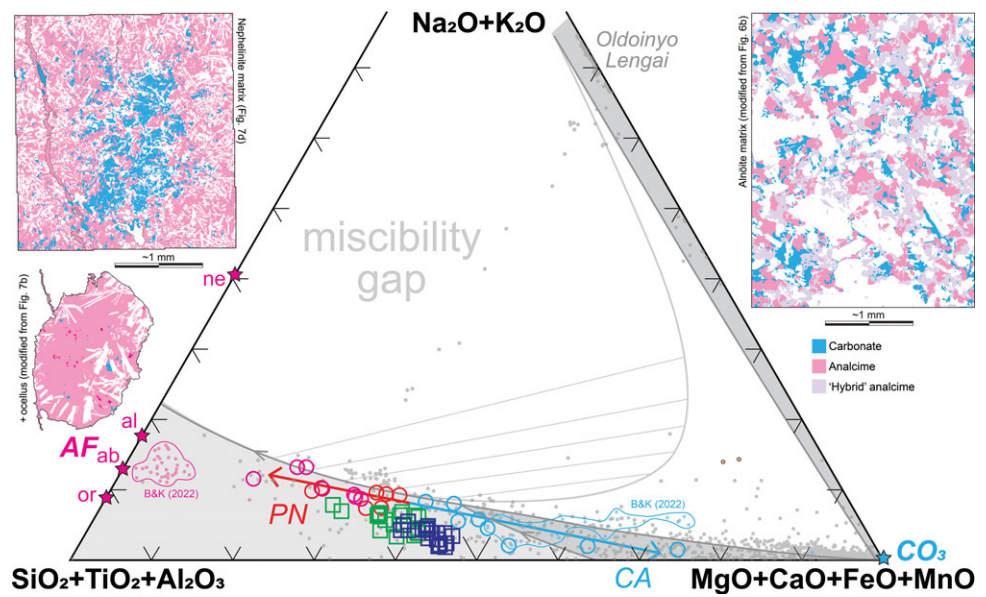
Figure 13. (Colour online) Ternary phase diagram under CO_2-saturated conditions, showing immiscible liquid alkali-carbonate and silicate solvus fields, according to both Brooker (1998, inner solvus with compositional tie lines) and a 10 kbar Hamilton diagram by Lee & Wyllie (1998), modified by Rosatelli et al. (2003). Sample symbols and other annotations as in Fig. 8, to which has been added a global data compilation by Berndt & Klemme (2022), as small symbols.

upper portion of the magma chamber, feeding aphyric LMD dykes and dyke margins.

The preferred source-tapping model just has a problem in explaining why HMD samples are overall more enriched than LMDs in Al_2O_3 and alkalis because low-density analcimic ocelli (thought to concentrate into HMD dyke cores) would not accumulate with denser mafic crystals but rather ascend to the top of the magma chamber. Thus, it is proposed that analcimic ocelli only started to exsolve once its magma chamber – as discussed next – gradually began to segregate into alnöites and nephelinites (cf., Fig. 12e). A similar delay would then also be expected inside dyke injected LMD and HMD magmas, where any late exsolution of less dense and larger anaclitic ocelli could then more readily flow segregate – as proposed earlier – into dyke core samples (Fig. 12b). Thus, a combination of both *in situ* flow segregation and source tapping is hereby envisaged, making it difficult to isolate specific diversification processes within lamprophyric complexes, especially, if combined source tapping and flow segregation operated from within a central source volume of multiple magma pockets.

5.c. Late-stage segregation into an alnöite–nephelinite suite

Compared to Larsen et al.'s (2009) geochemical survey of the Labrador Sea sub-province, FHI's more evolved T-trends stand out as either unique or similar alnöite and nephelinite intrusions are yet to be sampled and geochemically analysed from other lamprophyre–kimberlite–carbonatite complexes. In contrast, similar carbonatitic and nephelinitic dykes are also viewed as lamprophyric differentiates on the Kola Peninsular (Nosova et al. 2021a). Our study has further revealed how all sampled FHI dykes and sheets share both a convergence towards a common igneous centre (Fig. 2e) and sub-parallel incompatible element patterns (Fig. 11). Finally, while carbonatites are often regarded as complementary to lamprophyres and kimberlites, our geochemical results show how FHI's alnöite–nephelinite trends conform with such a carbonatitic end member. Thus, it seems permissible to speculate on a more important question: how FHI's alnöites and nephelinites differentiated from an evolved LMD parent?

The most important clues to the above question lie in how carbonatitic (CO_3) and alkali feldspathoidal (AF) end members to the alnöite–nephelinite suite, geochemically (Figs. 8–10 & 12a-b) bear such an uncanny resemblance to late-stage interstitial carbonate and analcime, respectively (Figs. 5g, 6, 7b, 8d & 12f), observed throughout all four of FHI's rock types. It is important to reinstate here that (1) FHI's rock types are insufficiently potassic to have formed leucite, which analcime appears to most commonly replace (e.g., Prelević et al., 2004, and references therein), (2) we have not found any indication of analcime precipitating as a secondary zeolite hydrothermal phase and (3) analcime rather appears to have crystallized either interstitially or in segregated veins and ocelli, as the latest igneous phase within the studied magmas. We do not know how these observations may be reconciled with Roux & Hamilton's (1976) experimentally constrained narrow stability field for igneous analcime, within a simpler nepheline-albite-water system, inside 6–13 kbar and 600–650°C, but still feel compelled to investigate how FHI's apparent analcime–carbonatite rest melts may have given rise to the alnöite–nephelinite suite. Especially, since (1) proportions of such interstitial phases increase from the analysed HMD thin section 519751 (32%), through alnöite sample 519745 (56%) to nephelinite sample 519715 (62%), while (2) carbonate versus analcime ratios differ between the alnöite (19:40, respectively, with an additional 41% of a hybrid Ca-Na-Si phase) and the nephelinite (9:91) sample (Table 3). However, while an increased total volume of interstitial phases, with relatively low liquidus temperatures, correlate with the degree of fractionation of first olivine, augite and magnetite, followed by kaersutite and biotite, and later possibly even apatite, perovskite, sanidine, nepheline, rutile and pyrite, identified as earlier crystals within more evolved rock types of this study (Figs. 4–7), it is less clear how mostly carbonatitic and analcime-rich rest melts segregated from each other.

Despite ample textural evidence of late-stage analcime and carbonatite forming bleb-like segregations, such apparent liquid immiscibility is not rigorously supported by any experimentally constrained liquid solvus involving analcime and carbonate. One established CO_2-rich solvus (e.g., by Brooker, 1998; Fig. 13) only explains how rare alkali carbonatites may exsolve from silicic melts,

and where a subsequent expulsion of late fenitizing alkali fluids is proposed to explain a global overabundance of calcic, magnesian and/or ferrous carbonatites (Bühn & Rankin, 1999; Kamenetsky *et al.* 2021; Yaxley *et al.* 2022). Nevertheless, Berndt & Klemme (2022) show how melt inclusions inside hauyne phenocrysts in phonolitic Lacher See lavas have exsolved carbonatitic bubbles inside alkali silicic envelopes, with compositions that are comparable to the calcite- and analcime-rich segregations described here for FHI (cf., 'K&B, 2022' in Fig. 13). Thus, it appears that some solvus must occur between such melts, but where it is unclear if this already exists across the less alkali edge of Brooker's (1998) solvus (base of ternary diagram in Fig. 13) or whether a more prominent solvus is yet to be experimentally constrained between alkali silicic and calcic/magnesian/ferrous carbonatite melts.

Early segregations could also have formed through a more wholesale magmatic process, as proposed by Ivanikov *et al.* (1998) and Panina & Motorina (2008) for similar rock types, as opposed to being entirely interstitial. In our case study, it just appears that segregation began after olivine, magnetite, augite, kaersutite, biotite, apatite and perovskite had crystallized and likely involved other elements, since melilites and rutiles concentrate inside carbonatitic domains, while nepheline and sanidine used up potassium within analcime-rich domains, crystallizing together with sulphides. According to variation diagrams (Figs. 8–10), CA – with a greater carbonatitic (CO_3) component – concentrated CaO, MgO, FeO, P_2O_5, REEs and most other incompatible elements, while PNs – with a greater AF component – concentrated more silica, aluminium and alkalis. It would also have been during such late-stage segregation that sanidine fractionated from within analcimic AF domains and thereby explain why SiO_2 and Al_2O_3 trends by LMDs do not consistently intersect where T-trends are subdivided into CA and PN samples (cf., 'or→' in Fig. 12a-b).

While Nosova *et al.* (2021b) note how ocelli and interstitial phases inside their damjernite samples are of similar compositions, FHI's ocelli and veins inside both a HMD (Fig. 6) and a nephelinite sample (Fig. 8b) all appear to be more analcime-rich than the interstitial analcime-to-carbonatite ratios recorded for corresponding matrixes (Table 3). This is supported by several reports of predominantly analcime-bearing ocelli (Carstens, 1961; Ferguson & Currie, 1971; Cooper, 1979; Foley, 1984; Lanyon & Le Roux, 1995; Keshava Prasad *et al.* 2001) of igneous origin. Analcime's apparent greater tendency over the carbonatitic rest melt component to form ocelli in the studied samples is puzzling but may relate to analcime's lower density, or greater buoyancy, leading to greater mobility, even if the carbonatitic component has a much lower viscosity than even hydrated analcime. A relatively stronger surface tension of analcime, compared to carbonatite, may also favour its ocelli formation, while a much lower viscosity of the carbonatitic component allows it to rather infiltrate the matrix of earlier crystallized phases, surrounding analcime-rich blebs (e.g., Fig. B7a) and even form irregular interstitial aggregates of their own (e.g., Fig. 7d). Otherwise, melt inclusions inside Hauyan phenocrysts of a Lacheer See phonolite indicate that immiscible carbonatite melts rather form bubbles inside immiscible alkali silicate melts (Berndt & Klemme, 2022).

From the above observations within relatively thin dykes and sheets that crystallized correspondingly fast, it may be imagined how similar late-stage segregations produced more refined and voluminous analcime and carbonatitic magma pockets inside more slowly cooled central magma chambers. As illustrated in Fig. 12(e), the evolved LMD top of a differentiating magma chamber could have had more time to segregate, with more buoyant and mobile analcime

rest melts ascending most rapidly to the top of chambers, if not farther up through their roof zones as veins. Such elevated, analcime-rich and hydrous rest melt accumulations would have a great potential of fenitizing host rocks, while also capping and insulting slightly denser carbonatites that either crystallized at depth and/or erupted. This is at least consistent with many carbonatitic volcanoes and intrusive centres (cf., Woolley & Kjarsgaard, 2008). Alternatively, intrusion of less completely segregated silico-carbonatite rest melts can also be envisaged, such as observed and modelled by Moore *et al.* (2022).

6. Conclusions

Radiating dykes and centrally inclined sheets of damtjernitic and more evolved CA and PN compositions all converge onto a positive aeromagnetic anomaly that resembles known carbonatite centres within other lamprophyre–kimberlite complexes across the southern west coast of Greenland and thereby potentially identifies a new carbonatitic centre for this FHI complex. The presence of such a carbonatite centre generates a remarkably regular spacing across the North Atlantic Craton, where carbonatites are typically located at terrane block centres and thereby questions an FHI terrane boundary between a southern Kvanefjord and northern Bjørnesund craton block.

Shared geochemical signatures provide further support for a cogenetic relationship between all converging dykes and sheets within this FHI complex. Porphyritic HMD and less phyric LMD subgroups – often as dyke cores and margins, respectively – define discordant bulk rock geochemical trends that were controlled by the accumulation of mainly augite, together with other mafic phenocrysts, while LMD trends require additional magnetite fractionation. It seems more likely for dykes to have first tapped differentiated LMD parts of an igneous centre, occasionally followed by the tapping of partially accumulated HMD mushes, excluding denser magnetite cumulates. Additional *in situ* flow segregation may, however, also have concentrated larger and lower-density ocelli into HMD dyke cores.

Bulk rock geochemistry of FHI's alnöite–nephelinite suite defines exceptional T-trend extensions from a more evolved LMD parent, which can only be explained through late-stage igneous segregations of interstitial carbonatitic and analcime-rich components, even if this segregation does not (yet) conform to any known immiscible solvus. Nevertheless, such segregations are observed as prevalent blebs, patches and zones in most alnöite and nephelinite dykes and sheets, as well as in more analcime-rich veins and ocelli in all rock types, including damtjernites. Inside a slower-cooled igneous centre, such segregations could potentially have generated more voluminous caps of purer analcime above denser carbonatite magma pockets and thereby offer a model for how non-alkali carbonatites form, at least within lamprophyre–kimberlite complexes.

References

Abersteiner A, Kamenetsky VS, Goemann K, Giuliani A, Howarth GH, Castillo-Oliver M, Thompson J, Kamenetsky M and Cherry A (2019) Composition and emplacement of the Benfontein kimberlite sill complex (Kimberley, South Africa): textural, petrographic and melt inclusion constraints. *Lithos* **324-325**, 297–314.

Barron LM (1996) Laminar flow, immiscibility and segregated fractionation in the Mt Townsend lamprophyric tephrite dyke, New South Wales: does flow change activities in the melt? *Australian Journal of Earth Sciences* **43**, 245–56.

Bell K (1989) *Carbonatite: Genesis and Evolution*. London, UK: Unwin Hyman, 618 p.

Bell K, Kjarsgaard BA and Simonetti A (1999) Carbonatites – into the twenty-first century. *Journal of Petrology* **39**, 1839–45.

Bergman S (1987) Lamproites and other potassium-rich igneous rocks: a review of their occurrence, mineralogy and geochemistry. *Geological Society, London, Special Publications* **30**, 103–90.

Berndt J and Klemme S (2022) Origin of carbonatites – liquid immiscibility caught in the act. *Nature Communications* **13**, 2892.

Brey GP, Bulatov VK, Girnis AV and Lahaye Y. (2008) Experimental melting of carbonated peridotite at 6-10 GPa. *Journal of Petrology* **49**, 797–821.

Brooker RA (1998) The effect of CO_2 saturation on immiscibility between silicate and carbonate liquids: an experimental study. *Journal of Petrology* **39**, 1905–15.

Brooker RA and Kjarsgaard BA (2011) Silicate-carbonate liquid immiscibility and phase relations in the system SiO_2-Na_2O-Al_2O_3-CaO-CO_2 at 0.1-2.5 GPa with applications to carbonatite genesis. *Journal of Petrology* **52**, 1281–305.

Bühn B. and Rankin AH (1999) Composition of natural, volatile-rich Na−Ca−REE−Sr carbonatitic fluids trapped in fluid inclusions. *Geochimica et Cosmochimica Acta* **63**, 3781–97.

Carstens H. (1961) A post-Caledonian Ultrabasic Biotite Lamprophyre Dyke of the Island Ytterøy in the Trondheimsfjord, Norway. *NGU Årsbok* **215**, 1–21.

Chadwick Jr WW and Dieterich JH (1991) Mechanical modelling of circumferential and radial dike intrusion on Galapagos volcanoes. *Journal of Volcanology and Geothermal Research* **66**, 37–52.

Cooper AF (1979) Petrology of ocellar lamprophyres from western otago, New Zealand. *Journal of Petrology* **20**, 139–63.

Dawson JB and Hawthorne JB (1973) Magmatic sedimentation and carbonatitic differentiation in Kimberlite sills at Benfontein, South Africa. *Journal of the Geological Society of London* **129**, 61–85.

Fareeduddin KIR and Basavalingu B (2001) Petrology of Ocellar Lamprophyres in South Delhi Fold Belt, Danva, Sirohi District, Rajastahn, India. *Gondwana Research* **4**, 497–508.

Ferguson J and Currie KL (1971) Evidence of Liquid immiscibility in alkaline ultrabasic dikes at Callander Bay, Ontario. *Journal of Petrology* **12**, 561–85.

Foley SF (1984) Liquid immiscibility and melt segregation in alkaline lamprophyres from Labrador. *Lithos* **17**, 127–37.

Garde AA, Hamilton MA, Chadwick B, Grocott J and McCaffrey KJW (2002) The Ketilidian orogen of South Greenland: geochronology, tectonics, magmatism, and fore-arc accretion during Paleoproterozoic oblique convergence. *Canadian journal of Earth Sciences* **39**, 765–93.

Giuliani A, Pearson DG, Soltys A, Dalton H, Phillips D, Foley SF, Lim E, Goemann K, Griffin WL and Mitchell RH (2020) Kimberlite genesis from a common primary melt modified by lithospheric mantle assimilation. *Science Advances* **6**, eaaz0424.

Hamilton DL, Freestone IC, Dawson JB and Donaldson CH (1979) Origin of carbonatites by liquid immiscibility. *Nature* **279**, 52–4.

Hansen K (1980) Lamprophyres and carbonatitic lamprophyres related to rifting of the Labrador Sea. *Lithos* **13**, 145–52.

Hansen K (1981) Systematic Sr-isotopic variation in alkaline rocks from West Greenland. *Lithos* **14**, 183–8.

Hansen K (1984) Rare earth abundances in Mesozoic undersaturated alkaline rocks from West Greenland. *Lithos* **17**, 77–85.

Harmer RE and Gittins J (1998) The case for primary, mantle-derived carbonatite magma. *Journal of Petrology* **39**, 1895–903.

Heaman LM and Kjarsgaard BA (2000) Timing of eastern North American kimberlite magmatism: continental extension of the Great Meteor hotspot track?. *Earth and Planetary Science Letters* **178**, 253–68.

Ivanikov VV, Rukhlov AS and Bell K (1998) Magmatic evolution of the melilitite – carbonatite – nephelinite dyke series of the Turiy Peninsula (Kandalaksha Bay, White Sea, Russia. *Journal of Petrology* **39**, 2043–59.

Kamenetsky VS, Doroshkevich AG, Elliot HAL and Zaitsev AN (2021) Carbonatites: contrasting, complex, and controversial. *Elements* **17**, 307–14.

Keshava Prasad AV, Beg MJ and Chatuvedi A (2001) Petrography of Lamprophyre Dikes from nunataks South of Schirmacher, Central Dronning Maud Land, East Antarctica. *Current Science Research Communications* **81**, 1477–1479.

Kjarsgaard BA (2007) Kimberlite diamond deposits. In *Mineral Deposits of Canada*, (ed. W Goodfellow) Geological Association of Canadian Mineral Deposits Division, Special Publication 5, pp. 245–72.

Kjarsgaard BA, Heaman LM, Sarkar C and Pearson DG (2017) The North America mid-Cretaceous kimberlite corridor: wet, edge-driven decompression melting of an OIB type deep mantle source. *Geochemistry Geophysics Geosystems* **18**, 2727–47.

Kokfelt TF, Weng WL and Willerslev E (2019) *Geological map of South and South West Greenland - 1:100,000*. Copenhagen: Geological Survey of Denmark and Greenland (GEUS).

Komar PD (1972) Mechanical interactions of phenocrysts and flow differentiation of igneous dikes and sills. *Geological Society of America Bulletin* **83**, 973–88.

Lanyon R and Le Roux AP (1995) Petrology of the alkaline and ultramafic lamprophyres associated with the Okenyenya igneous complex, northwestern Namibia. *South African Journal of Geology* **98**, 140–156.

Larsen LK, Heaman LM, Creaser RA, Duncan RA, Frei R and Hutchinson M (2009) Tectonomagmatic events during stretching and basin formation in the Labrador Sea and Davies Strait: evidence from age and composition of Mesozoic to Palaeogene dyke swarms in West Greenland. *Journal of the Geological Society, London* **166**, 999–1012.

Larsen LM and Rex DC (1992) A review of the 2500 Ma span of alkaline-ultramafic, potassic and carbonatitic magmatism in West Greenland. *Lithos* **28**, 367–402.

Lawver LA and Müller RD (1994) Iceland hotspot track. *Geology* **22**, 311–14.

Le Maitre RW (2002) *Igneous Rocks: A Classification and Glossary of Terms, Recommendations of the International Union of Geological Sciences, Subcommission of the Systematics of Igneous Rocks*. Cambridge University Press, 236 p.

Lee W-J and Wyllie PJ (1998) Petrogenesis of carbonatite magmas from mantle to crust, constrained by the system CaO – (MgO + FeO^*) – (Na_2O + K_2O) – (SiO_2 + Al_2O_3 + TiO_2) – CO_2. *Journal of Petrology* **39**, 495–517.

Mitchell RH (1994) The lamprophyre facies. *Mineralogy and Petrology* **51**, 137–46.

Mitchell RH (2005) Carbonatites and carbonatites and carbonatites. *Canadian Mineralogist* **43**, 2049–68.

Moore KR, Brady AE and Costanzo A (2022) Crystal-liquid segregation in silicocarbonatite magma leads to the formation of calcite carbonatite. *Journal of Petrology* **63**, 1–14.

Murphy JB (2013) Appinite suites: a record of the role of water in the genesis, transport, emplacement and crystallization of magma. *Earth-Science Reviews* **119**, 35–59.

Nosova AA, Kopylova MG, Sazonova LV, Vozniak AA, Kargin AV, Lebedeva NM, Volkova GD and Pertesetskaya EV (2021a) Petrology of lamprophyre dykes in the Kola Alkaline Carbonatite Province (N Europe). *Lithos* **398-399**, 106277.

Nosova AA, Sazonova LV, Kargin AV, Dubinina EO and Minervina EA (2021b) Mineralogy and geochemistry of ocelli in the damtjernite dykes and sills, chadobets uplift, siberian craton: evidence of the fluid–lamprophyric magma interaction. *Minerals* **11**, 724.

Nosova AA, Sazonova LV, Kargin AV, Smirnova MD, Lapin AV and Shcherbakov VD (2018) Olivine in ultramafic lamprophyres: chemistry, crystallization, and melt sources of Siberian Pre- and post-trap aillikites. *Contributions to Mineralogy and Petrology* **173**, 55.

Pandey R, Rao NVC, Dhote P, Pandit D, Choudhary AK, Sahoo S and Lehmann B (2018) Rift-associated ultramafic lamprophyre (damtjernite) from the middle part of the Lower Cretaceous 125 Ma) succession of Kutch, northwestern India: tectonomagmatic implications. *Geoscience Frontiers* **9**, 1883–902.

Panina LI and Motorina IV (2008) Liquid immiscibility in deep-seated magmas and the generation of carbonatite melts. *Geochemistry International* **46**, 448–64.

Pearson DG, Woodhead J and Janney PE (2019) Kimberlites as geochemical probes of earth's mantle. *Elements* **15**, 387–92.

Prelević D, Foley SF, Cvetković V and Romer RL (2004) The analcime problem and its impact on the geochemistry of ultrapotassic rocks from Serbia. *Mineralogical Magazine* **68**, 633–48.

Rock NMS (1987) The nature and origin of lamprophyres: an overview. *Geological Society, London, Special Publications* **30**, 191–226.

Rock NMS (1991) *Lamprophyres*. Glasgow, UK: Blackie, 285 pp.

Rosatelli G, Wall F and Le Bas J (2003) Potassic glass and calcite carbonatite in lapilli from extrusive carbonatites at Rangwa Caldera Complex, Kenya. *Mineralogical Magazine* **67**, 931–55.

Roux J and Hamilton D (1976) Primary igneous analcite; an experimental study. *Journal of Petrology* **17**, 244–57.

Sinclair GS, Barr S, Culshaw NS and Ketchum JWF (2002) Geochemistry and age of the Aillik Group and associated plutonic rocks, Makkovik Bay area, Labrador: implications for tectonic development of the Makkovik Province. *Canadian Journal of Earth Sciences* **39**, 731–48.

Stamm N and Schmidt MW (2017) Asthenospheric kimberlites: volatile contents and bulk compositions at 7 GPa. *Earth and Planetary Science Letters* **474**, 309–21.

Steenfelt A, Hollis JA and Secher K (2006) The Tikiusaaq carbonatite: a new Mesozoic intrusive complex in southern West Greenland. *Geological Survey of Denmark and Greenland Bulletin* **10**, 41–4.

Steenfelt A, Jensen MJ, Nielsen TFD and Sand KK (2009) Provinces of ultramafic lamprophyre dykes, kimberlite dykes and carbonatite in West Greenland characterised by minerals and chemical components in surface media. *Lithos* **112S**, 116–23.

Sun SS and McDonough WF (1989) Chemical and isotopic systematics of oceanic basalts; implications for mantle composition and processes. *Geological Society of London Special Publication* **42**, 313–45.

Tappe S, Brand NB, Stracke A, Van Acken D, Liu C-Z, Strass H, Wu F-Y, Luguet A and Mitchell RH (2017b) Plates or plumes in the origin of kimberlites: U/Pb perovskite and Sr-Nd-Hf-Os-C-O isotope constraints from the Superior craton (Canada). *Chemical Geology* **455**, 57–83.

Tappe S, Foley SF, Jenner GA, Heaman LM, Kjarsgaard BA, Romer RL, Stracke A, Joyce N and Hoefs J (2006) Genesis of ultramafic lamprophyres and carbonatites at Aillik Bay, labrador: a consequence of incipient lithospheric thinning beneath the North Atlantic Craton. *Journal of Petrology* **47**, 1261–315.

Tappe S, Foley SF, Jenner GA and Kjarsgaard BA (2005) Integrating ultramafic lamprophyres into the IUGS classification of igneous rocks: rationale and implications. *Journal of Petrology* **46**, 1893–900.

Tappe S, Foley SF, Kjarsgaard BA, Romer RL, Heaman LM, Stracke A and Jenner GA (2008) Between carbonatite and lamproite—Diamondiferous Torngat ultramafic lamprophyres formed by carbonate-fluxed melting of cratonic MARID-type metasomes. *Geochimica et Cosmochimica Acta* **72**, 3258–86.

Tappe S, Foley SF, Stracke A, Romer RL, Kjarsgaard BA, Heaman LM and Jouyce N (2007) Craton reactivation on the Labrador Sea margins: $^{40}Ar/^{39}Ar$ age and Sr–Nd–Hf–Pb isotope constraints from alkaline and carbonatite intrusives. *Earth and Planetary Science Letters* **256**, 433–54.

Tappe S, Kjarsgaard BA, Kurszlaukis S, Nowell GM and Phillips D (2014) Petrology and Nd-Hf isotope geochemistry of the neoproterozoic amon kimberlite sills, Baffin Island (Canada): evidence for deep mantle magmatic activity linked to supercontinent cycles. *Journal of Petrology* **55**, 2003–42.

Tappe S, Pearson DG, Kjarsgaard BA, Nowell GM and Dowall D (2013) Mantle transition zone input to kimberlite magmatism near a sub-duction zone: origin of anomalous Nd–Hf isotope systematics at Lac de Gras, Canada. *Earth and Planetary Science Letters* **371-372**, 235–51.

Tappe S, Pearson DG, Nowell G, Nielsen T, Milstead P and Muehlenbachs K (2011) A fresh isotopic look at Greenland kimberlites: cratonic mantle lithosphere imprint on deep source signal. *Earth and Planetary Science Letters* **305**, 235–48.

Tappe S, Romer RL, Stracke A, Steenfelt A, Smart KA, Muehlenbachs K and Torsvik TH (2017a) Sources and mobility of carbonate melts beneath cratons, with implications for deep carbon cycling, metasomatism and rift initiation. *Earth and Planetary Science Letters* **466**, 152–67.

Tappe S, Shaikh AM, Wilson AH and Stracke A (2021) Evolution of ultrapotassic volcanism on the Kaapvaal craton: deepening the orangeite versus lamproite debate. In *Lamprophyres, Lamproites and Related Rocks: Tracers to Supercontinent Cycles and Metallogenesis* (eds. L Krmíček and NV Chalapathi Rao. Geological Society, London, Special Publications **513**, pp. 17–44.

Tappe S, Steenfelt A, Heaman LM and Simonetti A (2009) The newly discovered Jurassic Tikiusaaq carbonatite-aillikite occurrence, West Greenland, and some remarks on carbonatite–kimberlite relationships. *Lithos* **112S**, 385–99.

Thomas MD, Ford KL and Keating P (2016) Review paper: exploration geophysics for intrusion-hosted rare metals. *Geophysical Prospecting* **64**, 1275–304.

Van Gool JAM, Connelly JN, Marker M and Mengel FC (2002) The Nagssugtoqidian Orogen of West Greenland: tectonic evolution and regional correlations from a West Greenland perspective. *Canadian Journal of Earth Sciences* **39**, 665–86.

Veter M, Foley SF, Mertz-Kraus R and Groschopf N (2017) Trace elements in olivine of ultramafic lamprophyres controlled by phlogopite-rich mineral assemblages in the mantle source. *Lithos* **292-293**, 81–95.

Weidendorfer D, Schmidt MW and Mattsson HB (2017) A common origin of carbonatite magmas. *Geology* **45**, 507–10.

White RS and McKenzie DP (1995) Mantle plumes and flood basalts. *Journal of Geophysical Research* **100** (B9), 17543–85.

Wilton DKC, Taylor RC, Sylvester PJ and Penney GY (2002) A review of kimberlitic and ultramafic lamprophyre intrusives from northern Labrador. Current Research, Newfoundland Department of Mines and Energy, Geological Survey, Report 02-1, 343–52.

Windley BF and Garde AA (2009) Arc-generated blocks with crustal sections in the North Atlantic craton of West Greenland: crustal growth in the Archean with modern analogues. *Earth Science Reviews* **93**, 1–30.

Woolley AR, Bergman SC, Edgar AD, Le Bas MJ, Mitchell RH, Rock NMS and Smith BHS (1996) Classification of lamprophyres, lamproites, kimberlites and the kalsilitic, melilitic and leucitic rocks. *The Canadian Mineralogist* **34**, 175–86.

Woolley AR and Kjarsgaard BA (2008) Carbonatite occurrences of the world: map and database. *Geological Survey of Canada Open File* **5796**, 28.

Yaxley MG, Anenburg M, Tappe S, Decree S and Guzmies T (2022) Carbonatites, classification, sources, evolution, and emplacement. *Annual Review of Earth and Planetary Sciences* **50**, 261–93.